STRUCTURAL LOADS ON WIND TURBINES OF INCREASING HEIGHT WITH CHANGES IN ATMOSPHERIC STRATIFICATION: A LARGE EDDY SIMULATION STUDY

by

Yohhan Dinkar Karkera

A thesis submitted to the faculty of
The University of Utah
in partial fulfillment of the requirements for the degree of

Master of Science

Department of Civil and Environmental Engineering

The University of Utah

December 2016

The University of Utah Graduate School

STATEMENT OF THESIS APPROVAL

The thesis of **Yohhan Dinkar Karkera**

has been approved by the following supervisory committee members:

Marc Calaf	, Chair	**05/05/2016** Date Approved
Luis F. Ibarra	, Member	**05/05/2016** Date Approved
Chris P. Pantelides	, Member	**05/05/2016** Date Approved

and by **Michael E. Barber** , Chair/Dean of

the Department/College/School of **Civil and Environmental Engineering**

and by David B. Kieda, Dean of The Graduate School.

ABSTRACT

Wind energy is one of the most rapidly growing sources of energy in the United States. With higher energy demands, next generation wind turbines will have larger blades and taller towers to increase the harvested power. However, in order to design taller towers, it is important to have a good understanding of how the wind flow interacts with turbines during operation. The aim of this research is to compute the loads on wind turbines for increasing heights under different atmospheric stratifications (convective, neutral, and stable) and within different turbine configurations (lone-standing wind turbine and turbine within a very large wind farm). To develop this study, an in-house numerical code has been used, capable of reproducing a realistic atmospheric flow as well as wind turbines. To compute the detailed turbine's rotor and tower loads, an additional open-source software developed by the National Renewable Energy Laboratory (NREL), so-called FAST, has been used. Streamwise wind turbine loads are computed, and the influence of different wind characteristics on the turbine's loads have been considered. We identify that wind velocity, turbulence, and wind shear play an important role on the wind turbine loads; the frequencies of the incoming wind velocity and rotation of the blades both affect the frequencies of the wind turbine loads. Results also show that the rotor thrust is the most dominant force acting on the wind turbine during the operational phase and has the strongest influence on the shear and bending moments of the wind turbine tower. From this

study, it is also found that by increasing the turbine tower height, power output can be increased by capturing energy from the low-level jet in the single wind turbine case, while for the wind farm case, improvements are minimal.

This thesis is dedicated to my beloved parents, who have been my eternal rock and source of refuge. I couldn’t be more grateful to Almighty for blessing me with such a great family. I could not have made it this far without you.

TABLE OF CONTENTS

LIST OF TABLES

LIST OF FIGURES

LIST OF ABBREVIATIONS

SWT – Single wind turbine.

WF – Wind farm.

CBL – Convective boundary layer.

NBL – Neutral boundary layer.

SBL – Stable boundary layer.

S90 – Single wind turbine case with a tower height of 90 m.

F90 – Wind farm case with a tower height of 90 m.

S150 – Single wind turbine case with a tower height of 150 m.

F150 – Wind farm case with a tower height of 150 m.

ACKNOWLEDGEMENTS

I would like to express my deepest appreciation to my committee chair, Dr. Marc Calaf, for having faith in my capabilities and giving me an opportunity to work in the exciting field of wind energy. This research would not have been possible without his guidance, patience, and encouragement throughout my time as a researcher.

I would also like to thank my committee members, Dr. Chris Pantelides and Dr. Luis Ibarra, for their valuable advice and guidance not only in my research, but throughout my time as a student at the University of Utah.

I am extremely thankful to Jason Jonkman and Bonnie Jonkman from the National Renewable Energy Laboratory, Colorado for their continued support and help regarding all my questions about FAST.

This research would not have been possible without the help of colleagues at the Wind, Energy and Turbulence Laboratory in the University of Utah. I am extremely grateful to Ph.D. student Gerard Cortina who has been of immense help in each and every step of this research. I would also like to thank Ph.D. students Fabien Margairaz and Travis Morrison for helping me understand the numerical simulations.

I feel blessed to have such great friends who have constantly supported, encouraged, and motivated me during my difficult times. I would like to thank Shreya, Zinnia, and Ashok for their encouragement and help with the programming aspects of this

study. Special thanks to my undergraduate friends, Priyank and Mazharali, for all their support and help in producing this manuscript.

CHAPTER 1

INTRODUCTION

1.1 A historical perspective of wind energy

Wind energy has been used extensively over the past 3000 years, primarily for grinding grain, pumping water, and in sailing ships. From as early as the thirteenth century, wind turbines were an integral part of the rural economy and only went into disuse with the advent of combustion engines and spread of rural electrification (*1*). The first wind turbine to generate electricity was a 12 kW DC windmill generator constructed by Brush, USA in the early nineteenth century. Research in the wind industry continued at a slow pace until the price of oil rose dramatically in 1973 (*1*). The sudden increase in oil prices stimulated a number of government-funded organization to research and develop new technologies in the wind industry. From 1973 until the mid-1980s, the U.S. government along with industry made efforts to expand wind energy technology. The U.S. in collaboration with the National Aeronautics and Space Administration, constructed a series of prototype turbines ranging from 100 kW Mod-0 in 1973 to 2.5MW Mod-5B in 1987. During this time, wind energy flourished, especially in California, partly because of federal and state tax incentives encouraging renewable energy. This trend in developing wind energy technology was also seen across the Atlantic, in countries like the U.K., Sweden, and Germany (*1*). In the early 1990s, however, wind energy suffered a major setback when

tax incentives ended and oil prices went down, thereby making electricity production from wind uneconomical, and hence slowing down the wind industry.

A renewed interest in the field of wind energy arises again today, with an added motivation being the need for a more affordable and clean source of electricity. Fossil fuels are neither renewable nor clean, and extraction and combustion generates air emissions, acid rain, water pollution, and, most importantly, CO_2 emissions, which are drivers of climate change. Global warming is on the rise, where the average temperature of our planet has risen by 1.4^{o} F since 1880 (*2*). Wind power is a commercially proven, rapidly growing form of electricity generation that provides clean, renewable, and cost-effective electricity around the world.

Over the past few years, the U.S. Department of Energy has shown a renewed interest in developing and improving wind turbine technology in the United States. According to the U.S. Department of Energy's Wind Vision 2015 Report (*3*), wind can help avoid the emission of over 250,000 metric tons of air pollutants, and greenhouse gases by 2050. In addition, wind has the potential to support over 600,000 jobs in manufacturing, installation, maintenance and supporting services by year 2050.

Currently, the U.S. Department of Energy (DOE) is targeting a 35% of the total energy to be produced by wind energy by the year 2050 (see Figure 1.1). According to the report (*3*), "the deployment of taller wind turbines with average height of 116 m will expand U.S land area available for wind deployment by 54%. Further innovation and increasing heights to 140 m will increase that further to 67%, and by achieving a height of 100 to 110 meters, wind energy can be open to all 50 states."

By the end of 2015, the U.S. had more than 74,000 megawatts (MW) of wind power

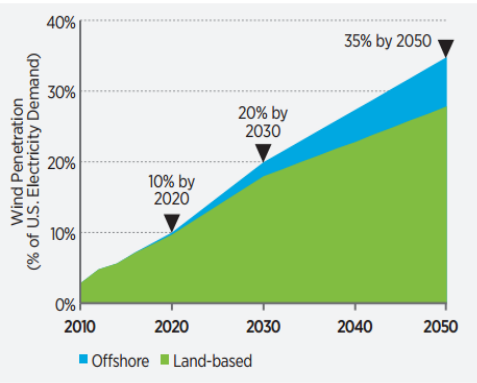

Cumulative Wind Capacity (GW)		2013	2020	2030	2050
Baseline Scenario	Land-based	61			
Central Study Scenario	Land-based	61	110	202	318
	Offshore	0	3	22	86
	Total	**61**	**113**	**224**	**404**

Figure 1.1. Wind penetration in the United States according to Wind Vision Report (*3*).

installed (see Figure 1.2), and currently, more than 18 million homes can be powered by this green electricity. Wind power generation in the U.S. grew at an average annual rate of 39% from 2004 through 2016. The State of Iowa now generates over 25% of its electricity from wind, and the State of Texas generates more than 9%. However, at present, only 4.7% of the total energy comes from wind energy in the United States. Worldwide, the growth rate in 2016 was over 17%, which makes wind one of the world's fastest growing forms of

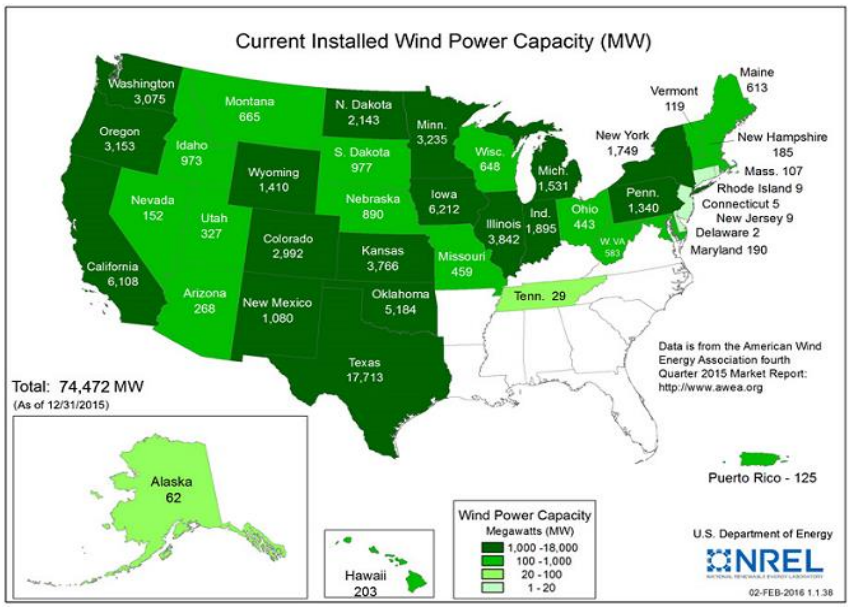

Figure 1.2. Installed wind power capacity in the United States (*4*).

power generation (*5*).

1.2. Research motivation

Wind energy has been a very active field of research since the beginning of the 20th century, with aerodynamics being one of the oldest branches of study within wind energy. Lanchester was the first person to predict the maximum power output of an ideal wind turbine in 1915 (*6*). A major breakthrough was made 20 years later, when Glauert proposed the blade element momentum theory (BEM), which is the most widely used technique to determine the aerodynamic loads on wind turbine blades, and to determine their power output (*7*). Over the years, improved BEM models considering yaw misalignment were proposed by Gaonkar (*8*) (1986), van Bussel (*9*) (1994), and Hansen (*10*) (1993), among others, and they have been used in works aiming to improve the wind turbine blade designs [Benini (*11*) (2002), Islam (*12*) (2008), Xudong (*13*) (2009)]. Also, wind turbine wakes' have been a topic of interest since the late seventies (*14*), with works focusing on the development of wake models for individual wind turbines as well as for large wind farms (*15,16,17,18,19,20*). For example, in 1979, Lissaman (*21*) considered for the first time the multiple wake interaction induced in very large wind farms. Katic et al. (*22*) (1986) pioneered research exploring varying wind farm configurations to improving the overall farm efficiency. This is currently a rich research topic and hence works have been published in the same topic by many others, such as Mosetti (*23*) (1994), Grady (*24*) (2005) and Chen (*25*) (2013), where binary algorithms were used to determine the most optimal wind farm layout in terms of cost and energy production. In each of these studies, they use a simplistic linear wake model to consider the wake effects instead of computational fluid dynamic models in order to reduce computational costs.

On the other end of wind energy research, there has also been important efforts to develop new and better structures for the wind turbine blades and the turbine tower. This is the result of the continuous increase in the size of the turbine rotor-disk and higher turbine's hub-height. Blades built of composite materials have been studied by Bechly (*26*) (1997), Ong (*27*) (2000), Kong (*28*) (2005), and Jensen (*29*) (2006), and turbine towers by Jay and Myers (*30*) (2014), among others, who proposed conical steel wind turbine towers that could be spirally rolled and welded on site. On the other hand, Sritharan (*31*) (2013) proposed concrete wind turbine towers made up of precast columns and panels made of ultra-high performance concrete. A comparison between steel and concrete towers of different heights and their feasibility has been studied by Quilligan (*32*) (2012). The study compares the structural performance of steel and prestressed concrete wind turbine towers ranging from 88 m to 120 m by comparing their maximum tower tip displacements. Concrete towers performed much better as compared to steel towers, and the authors conclude that concrete would be a much better option as compared to steel.

Interestingly, over the past few years, there has been an important parallel effort dedicated to improve our current understanding of the continuous interaction between wind turbines, their corresponding wakes, and the subjacent atmospheric flow. The study of the atmospheric flow close to the surface, the so-called atmospheric boundary layer (ABL), is an even older topic of research than wind energy itself. At the time, we have a deep understanding of the atmospheric mean properties as well as its turbulence structure from a statistical perspective [Gibson (*33*) (1798), Garratt (*34*) (1994) and Kaimal (*35*) (1994)]. A major advance in ABL research was the introduction of large eddy simulations (LES, explained in detail in Chapter 3) by Smagorinsky (*36*) (1963) and by the successive works

of Deordoff (*37*,*38*) (1972, 1974), Germano (*39*) (1991), and Lilly (*40*) (1992), which allow a numerical representation of the main turbulent characteristics of the ABL flow. For example, this numerical approach has allowed a better understanding of the differences in the ABL flow throughout a diurnal cycle, with the corresponding changes in atmospheric stability (seen later in Chapter 3).

Recently, LES have allowed developing more realistic studies of the wind turbine loads, considering full realistic atmospheric conditions. For example, Sim et al. (*41*) recently stated the need of efficient spatial and temporal resolution of simulated inflow wind fields to properly represent wind turbine dynamics and derive appropriate loads for accurate turbine designs. In their work, they studied three different inflow techniques, the conventional stochastic simulation, large-eddy simulation, and large-eddy simulation with fractal interpolation for a neutrally stratified boundary layer (NBL). The simulations were run for 12 ms^{-1}, 15 ms^{-1}, and 18 ms^{-1}, and the highest loads were only obtained for the 12 ms^{-1}case. Their findings suggested that an inflow wind field with a grid spacing around one-tenth of the rotor diameter and 1 Hz frequency should be adequate for load studies. Also, Park et al. (*42*) have argued that stochastic simulations of turbulent inflow fields used in wind turbine load computations cannot account for the varying atmospheric stratification and characteristics. They propose that LES-generated wind fields should be used for load computations since they take into consideration important wind characteristics such as enhanced wind speed and directional wind shear. In their study, a total of 50 LES simulations were run, which accounted for a large variability on different flow characteristics such as mean geostrophic wind, surface roughness, surface cooling rate, initial boundary layer height, the Coriolis parameter and the corresponding

geostrophic departure. Their LES domain was 800 m x 800 m x 790 m in the x, y and z directions, correspondingly, and had a spatial and temporal resolution of 10 m and 10 Hz, respectively. In that study, wind loads were obtained using the aero-elastic simulation code, FAST (seen later in Chapter 4). Out-of plane bending moment (OoPBM), tower top yaw moment (TTYM) and fore-aft tower bending moment (FATBM) are the three loads that were studied. The increase in wind speed shear was shown to have strong influence on the blade root out-of plane bending moment (OoPBM) of the wind turbine. Also, an increase in geostrophic wind speed led to increased standard deviation and mean of the longitudinal hub-height wind speed. Increase in surface cooling rate enhanced the wind shear and also increased the hub mean speed, which also led to decreased fatigue and higher TTYM and FATBM. In another study, Park et al. (*43*) tried to investigate whether wind field characteristics associated with the stable boundary layer (SBL) could be reproduced by using simpler stochastic simulation approaches (similar to the one mentioned in International Electrotechnical Commission (IEC) guidelines (*44*)) by making appropriate corrections for shear, veer, turbulence etc. The authors compared LES-generated SBL flow fields with the modified stochastic NBL flow fields in order to isolate distinguishing characteristics of wind shear, wind veer and turbulence variation over the rotor plane. They also computed and compared the associated loads for the NREL 5 MW turbine for both the SBL and the NBL wind fields. In conclusion, they state that for an accurate representation of the conditions in the SBL, LES-type-generated wind fields are required.

With wind turbines reaching taller heights, the wind turbine tower becomes as important as the rest of the wind turbine system. The loads on the wind turbine tower

increase tremendously with increasing heights. Also, blade sizes increase in proportion to the increase in height; hence, the wind turbine towers have to support this extra weight. Among the costs of a wind turbine system, the wind turbine tower cost may constitute as much as 30% of an entire megawatt-scale horizontal axis wind turbine, and about 10% of the total cost of energy (*32, 45*). On an average, it costs an additional $15,000 to increase the height of the wind turbine by 10 m (*45*). However, prior to installing such tall turbines, it is important to understand the interaction between the wind flow and wind turbines under different atmospheric stratification at these higher heights. How will the loads on the wind turbine tower change as we go taller? How do the loads vary with different wind turbine configurations? Will increasing turbine heights have a significant increase in power output? The answers to these questions need to be known before proceeding with next steps.

Wind turbine towers are designed according to the guidelines provided in the International Electrotechnical Commission 61400-1 Design Handbook (*44*). However, these guidelines follow a simplistic approach and do not take into account a number of atmospheric boundary layer dynamics, such as enhanced wind shear, the low-level jet, wind direction changes and different atmospheric stratifications. Although Park et al. (*42, 43*) have simulated loads for wind turbines under SBL and NBL conditions, their study is limited to a single wind turbine with a tower height of 90 m. Their work does not explore the effects of upstream wakes on the loads of wind turbines placed in a wind farm. Also, there are no studies that have yet focused on studying the operational loads arising on wind turbines placed at different heights. Hence, the aim of this research is to study the interaction of wind turbines, both when installed standing alone or within a wind farm,

with the atmospheric flow as a function of increasing turbine height. The corresponding turbine loads will be computed for regular turbine working conditions, covering the three most important periods of a diurnal cycle: day time (Convective boundary layer), night-time (Stable boundary layer) and neutral conditions (Neutral boundary layer).

1.3 Research goals

This thesis research goals include:

- Create new understanding of the interaction between wind turbines (in both, a large wind farm and a single wind turbine configuration) and the atmospheric flow under different stratifications (stable, neutral, unstable) with changes in wind turbine heights (90-150 m).
- Compute the loads on the wind turbine rotor and tower for the above-mentioned cases.
- Quantify the changes in harvested power between the cases mentioned and investigate the potential benefits of higher wind turbines.
- Compare the shear force and bending moment on the wind turbine's tower for the different cases.

1.4. Research organization

Chapter 2 provides a brief description of the ABL and the numerical technique used to describe it. Chapter 3 provides an introduction to the LES technique, the numerical model used to describe the wind turbine as well as an overview of the different types of loads acting on a wind turbine. Chapter 4 presents the different study cases used in this study.

The results are presented in Chapter 5 and Chapter 6 includes a detailed discussion. Finally, the concluding remarks are presented in Chapter 7.

CHAPTER 2

INTRODUCTION TO ATMOSPHERIC BOUNDARY LAYER AND COMPUTATIONAL FLUID DYNAMICS

2.1. Atmospheric boundary layer

The earth's atmosphere is more than 100 km thick, but the weather systems such as cyclones, storms and hurricanes hardly occupy more than the bottom 10 km, a layer called the troposphere. The atmospheric boundary layer is around 1-2 kilometers thick and forms the lower-most layer of the troposphere. The interaction between the surface and the air occurs in two forms, mechanical and thermal. The mechanical contact arises due to the friction exerted by the wind against the ground surface, which causes the wind to be sheared and thus creating turbulence. The thermal contact occurs due to the temperature differences between the surface of the earth (heated by the sun) and the air above. During a normal diurnal cycle, a cycle of changes in the temperature, humidity and winds are typically observed, which are governed by the dynamics and physics of the atmospheric boundary layer. During daytime, the temperature is higher and the flow tends to be strongly turbulent, whereas during night time, temperatures are cooler and the flow is calmer, at least close to the surface. The boundary layer is said to be convective or unstable (CBL) when the surface is warmer than the air above. This is generally observed during a sunny day with weak winds blowing over land. During this period, the flow is well mixing up to a considerable

height. This height generally varies between 1 and 2 kilometers, defining the height of the ABL. Figure 2.1 schematically shows the structure of the convective ABL under clear skies. The boundary layer is said to be stable when the surface is cooler than the air above, which is traditionally observed during night time. The primary cause of turbulence in the stable boundary layer (SBL) is the shear near the earth's surface. The thickness of this layer depends on the prevailing wind velocity as well as on the roughness of the surface, but it rarely exceeds 300 m. Also, a neutral boundary layer (NBL) can be observed, both during the transition between the CBL and the SBL and in cases of strong winds with strong mixing.

The evolution of a traditional diurnal cycle of the ABL is as follows: early in the morning, when the sun rises, the air close to the surface begins to heat from below and

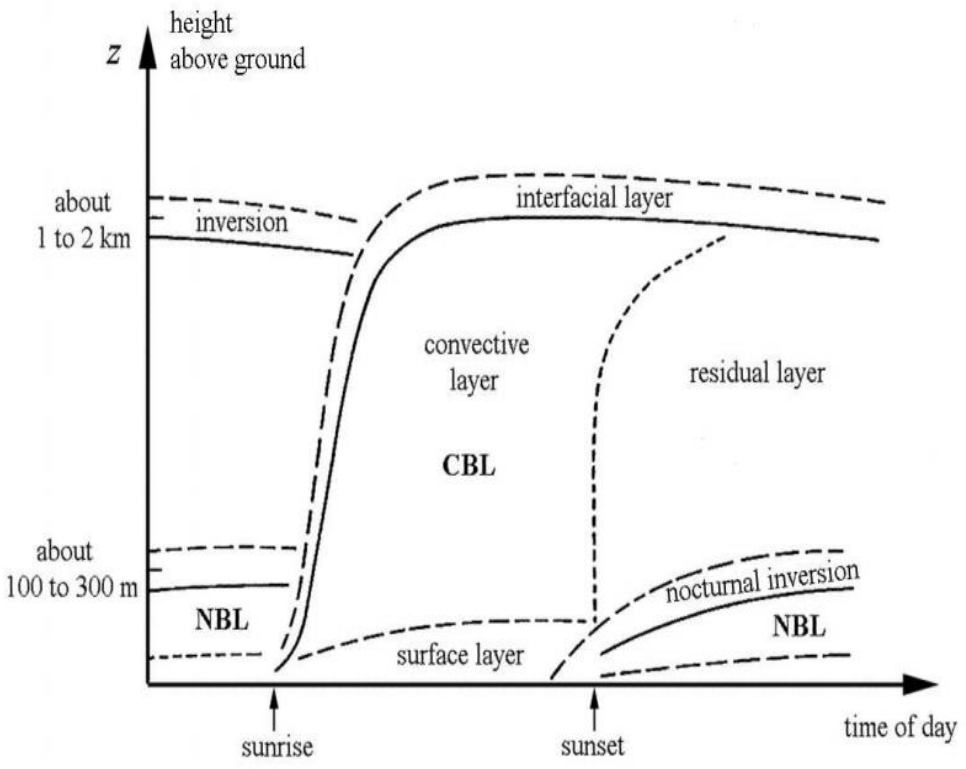

Figure 2.1. Typical evolution of the atmospheric boundary layer in a diurnal cycle (*34*).

convective motions progressively develop, inducing vertical mixing. A progressive increase in convection follows, gradually eroding upwards the stratified layer created during the night. At this time, shear-induced turbulence is weaker than the convection-induced turbulence, except at the base of the CBL, where both have a similar effect. This lower region is known as the surface layer (see Figure 2.1). With time, the height of the CBL increases until late afternoon. With the decay of solar radiation, the CBL loses energy (misbalance between the residual turbulence that dissipates energy and the lack of new input from the surface) evolving towards the so-called residual layer. With the progressive cooling of the surface, thermal turbulence is damped and a new stable boundary layer is formed, topped by the residual layer, whose energy will progressively decay. As earlier mentioned, the stable boundary layer (SBL) is characterized by weak turbulence (produced by surface shear), with sporadic bursts of high intensity turbulence (due to vertical intrusions of gravity waves or other large-scale atmospheric perturbations) (*46*, *47*, *48*).

2.2 Computational fluid dynamics and turbulence modeling

Structural engineers generally consider wind to increase in a parabolic trend with height as mentioned in the design guidelines given by ASCE 7 and IBC (*49, 50*). The IEC 61400-1 describes the wind speed profile within the turbine rotor layer by a power law (*44*),

$$U(z) = U_h \left(\frac{z}{z_h}\right)^{\alpha}$$

where U_h is the wind speed at the wind turbine hub-height (z_h), $U(z)$ is the wind speed at height z and α is the shear exponent which is equal to 0.2. However, in reality, wind behaves much differently, with strong variability according to the changes in atmospheric stratification. The power law assumes the atmospheric boundary layer to be always neutral

which while being a decent approximation in most cases, is far from accurate most of the time. During a convective boundary layer, wind shear is low and the flow is turbulent, whereas during the stable boundary layer, wind is accompanied by a strong wind shear and less turbulence. Also at night time, the flow can be characterized by the presence of the so-called low-level jet (LLJ, typically formed between 100 – 500 m from the ground), which consists of a narrow band of air that moves with a super-geostrophic wind speed. The geostrophic wind speed is the mean velocity of the flow at the top of the ABL, and is the forcing engine of the atmospheric boundary layer from the top. As will be shown later (Chapter 4), and has already been illustrated by Rife et al. (*51*), the changes in the wind speed are important and should be considered to design the most optimal wind turbine.

Computational fluids dynamics (CFD) is a branch of fluid mechanics that describes numerical methods to integrate the equations of motion for fluids (the Navier-Stokes equations in case of an incompressible flow), and hence provide a method to visualize, understand and quantify the fluid characteristics and behavior under different conditions. In this study, CFD are used to study the atmospheric flow around wind turbines. Over the years, many CFD techniques have been proposed and developed, providing more-or-less accurate descriptions of flow field with time (*52*). For example, direct numerical simulations (DNS), Reynolds-averaged Navier-Stokes (RANS) equations and Large Eddy Simulation (LES) are the three most widely used turbulence modeling techniques. DNS provides the complete description of the flow. However, for these to be correct, it is necessary to numerically resolve all the turbulent structures of the flow, and hence, very fine numerical resolution down to the millimeter scale is needed. At the same time, it is also necessary that the domain is large enough to enclose the largest turbulent eddies, which

scale with the Reynolds number (Re) of the flow. The Reynolds number is a nondimensional number that relates the shear forces with the viscous forces of the flow, and the largest turbulent eddies scale proportional to the Reynolds number (Re = U*L/viscosity). Hence, the larger the Re, the larger are the biggest turbulent eddies (L) and hence, the bigger the numerical domain needs to be. In the case one wants to numerically integrate the atmospheric flow, it is not possible to use DNS because the Re is approximately of 10^6, and hence, it would require about 10^{18} grid points for accurately solving for all the turbulent eddies forming the flow (*52*). To overcome this difficulty, LES was developed by Smagorinsky in 1967 (*36*). LES reduces the computational cost as a result of a filtering process that eliminates the need to resolve the smaller turbulent eddies. These are instead parameterized by means of more-or-less advanced models. The numerical filtering separates those turbulent eddies carrying most of the energy and hence requiring to be solved for to reproduce the most important characteristics of the real flow, and those which only transfer energy down into the turbulence energy cascade and dissipate the turbulent energy into heat, and therefore can be modelled. In this research project, we will be using an in-house LES code capable of reproducing the atmospheric flow throughout a diurnal cycle which will be used to study the loads arising on the structure of the wind turbine. This code is discussed in detail in Chapter 3.

CHAPTER 3

LARGE EDDY SIMULATION OF THE ATMOSPHERIC BOUNDARY LAYER AND WIND TURBINE MODELLING

3.1 Large eddy simulation of the ABL

In LES, the large-scale eddies (or energy containing eddies) of a turbulent flow are computed directly, and only the subgrid-scale (unresolved) eddies are modelled (see Figure 3.1). This scale separation is obtained through either an implicit or an explicit filter. In this specific work, the governing equations for an incompressible flow, the so-called Navier–Stokes (NS) equations, are implicitly filtered by the numerical grid resolution (equivalent to applying a box-type filter).

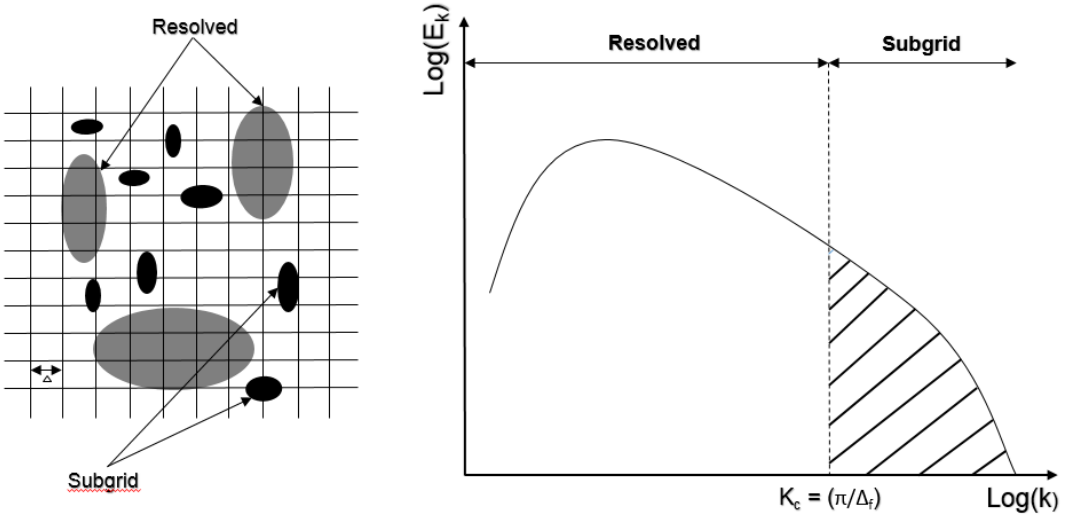

Figure 3.1. Resolved and subgrid scales of LES showed in physical (left) and Fourier space (right) (Adapted from Park et al. (*43*)).

In this work, the LES code introduced in Sharma et al. (*53*) is used, which solves the nondimensional, filtered NS equations for an incompressible flow in hydrostatic equilibrium together with the filtered equation for conservation of mass. The rotational form of the Navier-Strokes equations is used in order to ensure conservation of mass and energy of the inertial terms (*54*). The effect of temperature has been introduced into the momentum equations using a thermal buoyancy term as a result of using the Boussinesq approximation. The full set of equations being solved is therefore,

$$\frac{\partial \tilde{u}_i}{\partial x_i} = 0 \tag{3.1}$$

$$\frac{\partial \tilde{u}_i}{\partial_t} + \tilde{u}_j \left(\frac{\partial \tilde{u}_i}{\partial \tilde{x}_j} - \frac{\partial \tilde{u}_j}{\partial \tilde{x}_i}\right) = -\frac{1}{\rho}\frac{\partial \tilde{p}}{\partial x_i} - \frac{\partial \tilde{\tau}_{ij}}{\partial x_j} + g\left(\frac{\tilde{\theta} - \hat{\tilde{\theta}}}{\hat{\tilde{\theta}}}\right) + f(\tilde{u}_2 - \vartheta_G)\delta_{i_1} - f(\tilde{u}_1 - u_G)\delta_{i_2} + f_i \tag{3.2}$$

$$\frac{\partial \tilde{\theta}}{\partial t} + \tilde{u}_j \frac{\partial \tilde{\theta}}{\partial x_j} = -\frac{\partial \pi_j}{\partial x_j} \tag{3.3}$$

where $\tilde{\theta}$ is the filtered potential temperature, $\tilde{u}_i$ is the LES-filtered velocity component in the *i* direction (*i* = 1,2,3) and $\tilde{p}$ is the resolved dynamic pressure term. The deviatoric part of the momentum subgrid stress term $\tau_{i,j}$ is modelled with the Lagrangian scale-dependent model of Bou-Zeid et al. (*55*) and the corresponding subgrid scalar flux of potential temperature is modelled using the adaptation of the Lagrangian scale-dependent model for scalars introduced in Calaf et al. (*56*). Terms u_G and ϑ_G represent the streamwise and spanwise components of the geostropic wind, and f is the Coriolis factor, which is latitude dependent. The tilde (~) in the equations represents the LES filtering at grid size (Δ), and (^) represents a secondary filtering operation at a spacing twice the grid size (2Δ). In Equation (3.2), δij is the Kronecker delta (δij=1 for $i = j$, 0 otherwise). The effect of atmospheric stratification is introduced by the potential temperature which acts as an active scalar to modify the buoyancy of the air, thus enhancing vertical displacements of air

parcels and the momentum equation. This is introduced using the Boussinesq approximation in Equation (3.2) for the potential temperature. The effect of the wind turbines is introduced by a combination of a drag force and a tangential force through the f_i term. The numerical discretization of the equations is adapted from Moeng (*57*) and Albertson et al. (*58, 59*). Fourier-based methods are used in both horizontal directions, which makes the domain fully periodic, and thus no lateral boundary conditions are needed. In other words, the domain tends to infinity in the horizontal directions. Time integration is carried out using the second-order Adams-Bashforth scheme. The nonlinear convective terms are dealiazed with the 3/2 rule (*60*). Vertical velocity and gradients of velocity and temperature are set to zero at the top boundary condition. For the surface boundary conditions, a nonslip condition is imposed for the vertical velocity, and for the horizontal components of the momentum equation, an equivalent shear stress is imposed using the law of the wall with atmospheric stability correction,

$$\tau_{i,3}(x, y, z_1) = -\left[\frac{k\sqrt{(\widehat{\tilde{u}}_1^2 + \widehat{\tilde{u}}_2^2)}}{\ln(z_1/z_0) + \varphi_m(z_1/L)}\right]^2 n_i \tag{3.4}$$

In the above equation, i is the specific direction in the plane parallel to the surface (i = 1,2) and n_i is a unitary directional vector, given by $n_i = \frac{\widehat{\tilde{u}}_1}{\sqrt{\widehat{\tilde{u}}_1^2 + \widehat{\tilde{u}}_2^2}}$. The surface roughness is constant over the entire numerical domain and has been set to z_0 = 0.1 m. This value corresponds to a ground surface with low crops (*47*). For the numerical integration of the momentum equation, the vertical derivatives of the horizontal velocity components are also needed. These are parameterized at the first grid point also using Monin–Obukhov similarity theory (*61*),

$$\partial_3 \tilde{u}_i(x, y, z_1) = \left(\frac{\sqrt{\tau}}{kz}\right) n_i \tag{3.5}$$

with $\tau = \sqrt{\tau^2{}_{1,3} + \tau^2{}_{2,3}}$. In a similar fashion as for the momentum, the kinematic sensible heat flux is computed at the first staggered grid point using Monin–Obukhov similarity theory,

$$H_s\,(x, y, z_1) = \frac{K^2[\theta_s - \tilde{\theta}\,(x,y,z_1)]\left(\sqrt{(\tilde{u}_1^2 + \tilde{u}_2^2}\right)}{[ln\,(z_1/z_0) + \varphi_m\,(z/L)]\,[ln\,(z_1/z_{0,h}) + \varphi_h\,(z/L)]} \tag{3.6}$$

where the surface temperature (θ_s) is imposed as bottom boundary condition. The stability correction functions (φ) implemented are adopted from Brutsaert (*62*). Different formulations exist depending upon stability, and the appropriate choice of functions is made based upon the Obukhov length (L), which is given by,

$$L = \frac{-u_*^3\,\bar{\theta}_s}{k\,g\,\overline{w'\theta'_s}} \tag{3.7}$$

where $u_\star$ is the friction velocity, $\bar{\theta}$ the mean potential temperature, κ the de von Kármán constant (κ = 0.4) and $\overline{w'\theta'}$ is the surface sensible heat flux. In this work, the scalar surface roughness has been taken to be one-tenth of the momentum surface roughness ($z_{0,h}$=z_0/10) (*63*). Figure 3.2 shows a typical representation of a LES domain.

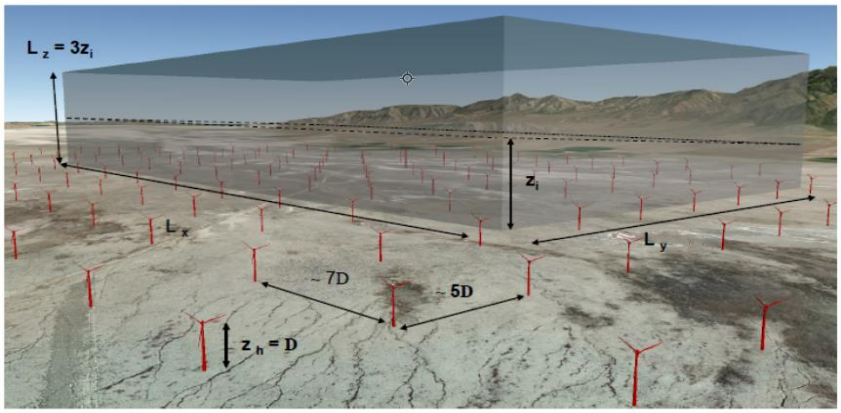

Figure 3.2. LES domain representation for a wind farm (D=Rotor Diameter, zh = hub-height, zi = top of boundary layer).

3.2 Wind turbine model

The wind turbine model in the LES is adapted from Sharma et al. (*53*), where turbines are introduced in the LES domain by including additional body forces in the NS equations. This force is computed using the actuator disk concept (see Figure 3.3), which states that a wind turbine induces a drag force proportional to the square of the unperturbed incoming wind velocity (u_d), the area swept by the rotor and the thrust coefficient, C_T. A tangential force is also introduced in the model to study the near wake characteristics of the wind turbine. Hence, the two forces introduced in the wind turbine model are,

$$f_t = -\frac{1}{2}\rho C'_T \langle \tilde{u} \rangle^2{}_d \tag{3.8}$$

$$f_\theta = \frac{1}{2}\rho C'_P \langle \tilde{u} \rangle^2{}_d \ \frac{\langle u \rangle_d}{\Omega r} \tag{3.9}$$

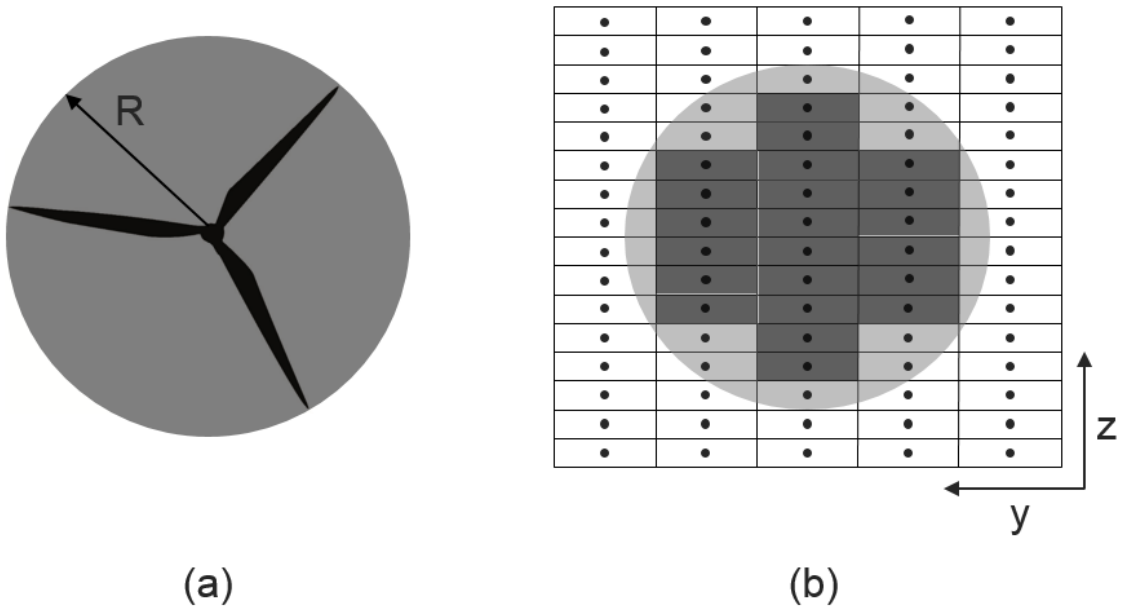

Figure 3.3. Wind turbine model in LES (a) Classic actuator disk scheme (b) Numerical decomposition of the actuator disk on a regular LES grid (Adapted from Sharma et al. (*53*)).

where f_t is the standard drag force per unit area and f_θ is the tangential force per unit area at distance r from the center. The actual force can be obtained by multiplying equations (3.8) and (3.9) by the element area, $r\ dr\ d\theta$. In the real world, wind turbines align themselves in line with the flow, an important aspect that is replicated by this model wherein the wind turbines reorient every 10 minutes in the direction of the mean flow. For a detailed description of the wind turbine model; refer to Sharma et al. (*53*).

3.3 In-plane velocity using a characteristic box tool

To directly compare the flow around a single wind turbine (SWT) and the flow around a wind turbine installed within a wind farm (WF), a dynamically time-realigned control volume surrounding each wind turbine has been designed within this project, which is referred to as the characteristic wind turbine box. The characteristic box consists of a reduced control volume of adjustable size, with the box-local streamwise direction timely aligned perpendicular to the actual rotor disk (see Figure 3.4). This wind turbine characteristic box provides a unique opportunity to compare flow statistics around an isolated wind turbine and a turbine within a large wind farm, and in this research project will be used to extract the necessary inflow data to compute the corresponding wind turbine loads (see later in Chapter 5).

The characteristic box is centered around the rotor, with an X and Y dimension of 5D and 9D, respectively. Precisely in this work, the box extends between a distance of 2D-upstream and 7D, downstream of the disk in the streamwise direction, and 2.5D left and right of the hub of the rotor in the cross-streamwise direction, respectively. In the vertical direction, the box height has been varied. The box size allows us to capture

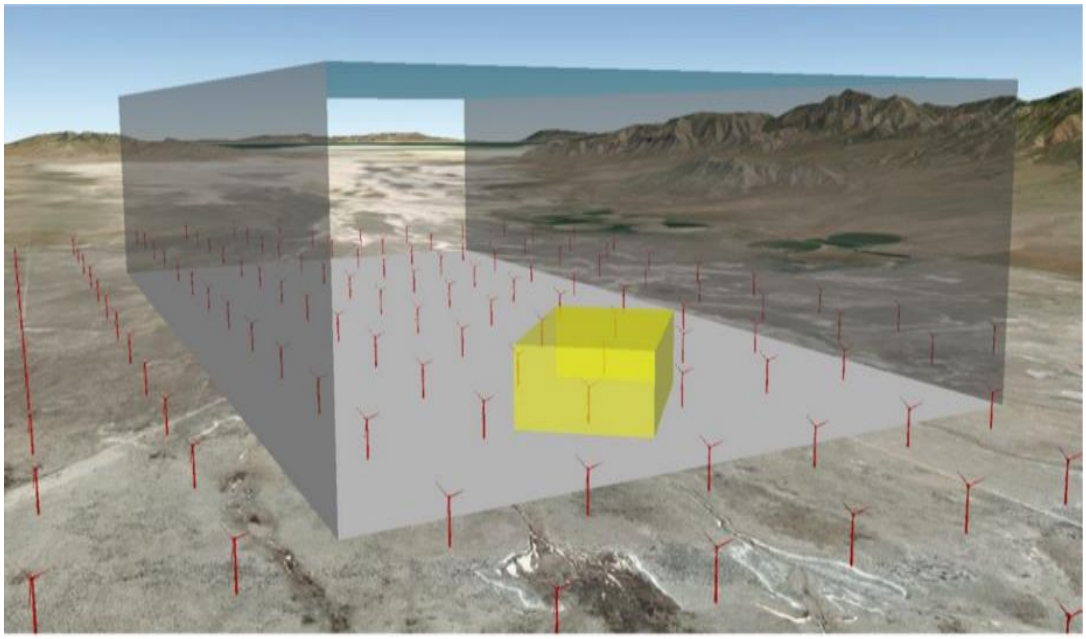

Figure 3.4. Characteristic box representation inside the LES domain.

properly the flow around an individual wind turbine, in both the SWT and WF cases. The wind turbine box is designed such that its corresponding streamwise axis (x_b) is timely perpendicular to the rotor disk, and hence aligned with the mean wind vector. The flow variables are initially computed within the base LES coordinate frame (x_{LES}, y_{LES}, z_{LES}) and then transformed into the new box coordinate frame (x_b, y_b, z_b). The mapping transformation consists of a rotation around the vertical axis ($z_{LES} = z_b$), which remains frame invariant and it is represented by the rotation matrix R,

$$R = \begin{bmatrix} cos\phi & sin\phi & 0 \\ -sin\phi & cos\phi & 0 \\ 0 & 0 & 1 \end{bmatrix}$$

where ϕ is the horizontal angle between the LES domain and the box coordinate system (see Figure 3.5). Note that through the resultant coordinate transformation, the LES mean flow direction becomes the box local streamwise direction ($u_b = R\ u_{LES}$). Similarly, the Reynolds stress tensor components are transformed using the corresponding matrix.

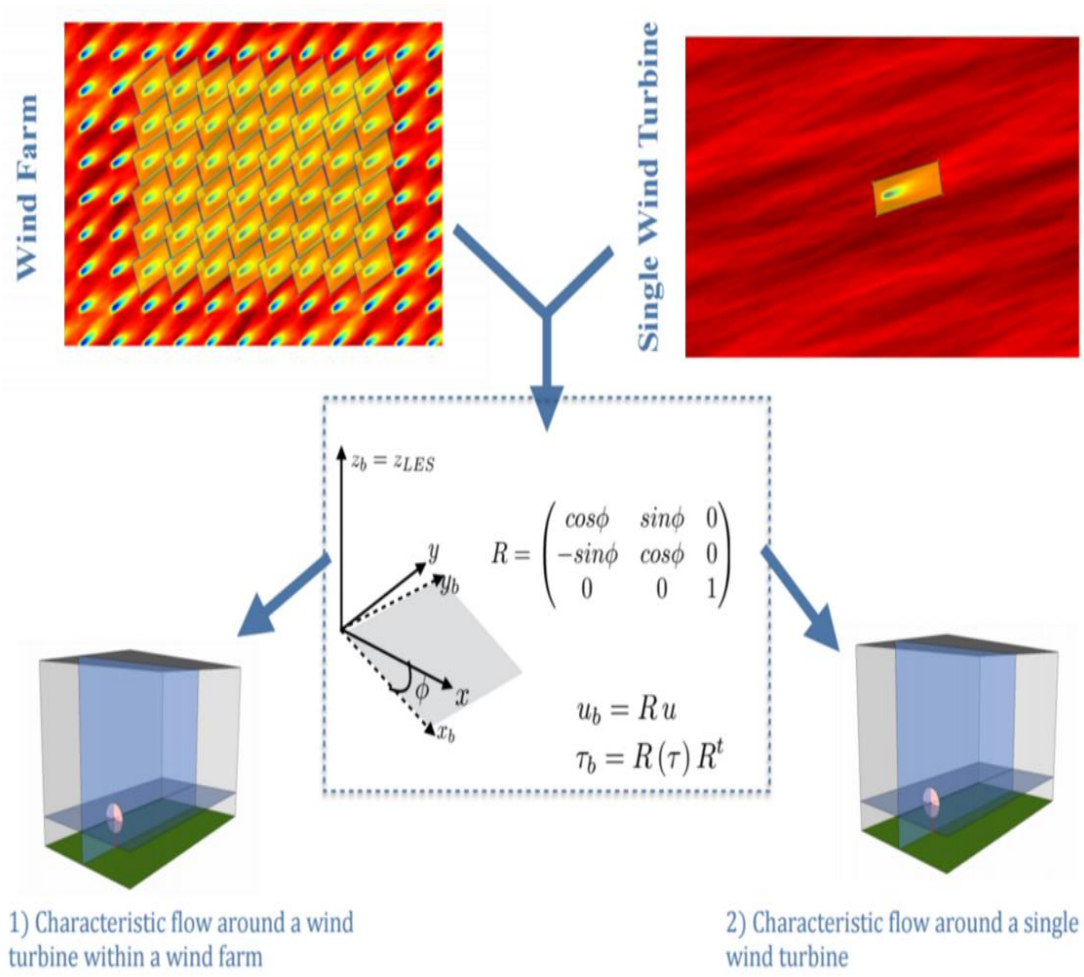

Figure 3.5. Flow-chart representing generation of characteristic box from LES domain.

transformation $\tau_{box} = R\ \tau_{LES}\ R^T$, where R^T indicates the transpose of the rotation matrix. Figure 3.5 illustrates the structure of the wind turbine box within the LES domain for the SWT and WF cases, respectively, and the schematics of the frame rotation $(x_{LES}, y_{LES}, z_{LES}) \rightarrow (x_b, y_b, z_b)$. The box tool plays an important role in obtaining streamwise velocities perpendicular to the wind turbine rotor. It also helps in comparing output variables between a wind turbine placed in isolation and a characteristic wind turbine placed in a wind farm. The use of the wind turbine box will become very valuable when evaluating the loads on the wind turbines (seen later in Chapter 5).

3.4. Loads on the wind turbine

A wind turbine throughout its life cycle experiences a variety of static, dynamic, and fatigue loads. Wind loads on the wind turbine can be classified into two main types, wind turbine rotor or blade loads and tower loads. In this study, using the NREL onshore 5-MW baseline wind turbine model, we compute the rotor loads using the turbine inflow data obtained from the LES simulations together with the aero-elastic simulation code FAST (*64*), which computes the detailed turbine loads'. The tower loads are computed using a combination of FAST and the conventional drag force equation used in Quilligan et al. (*32*). In Figure 3.6, a graphical representation of the steps involved to compute the rotor loads using Large eddy simulation and FAST is presented. A detailed explanation of the rotor loads and its computation will be presented in the next sections.

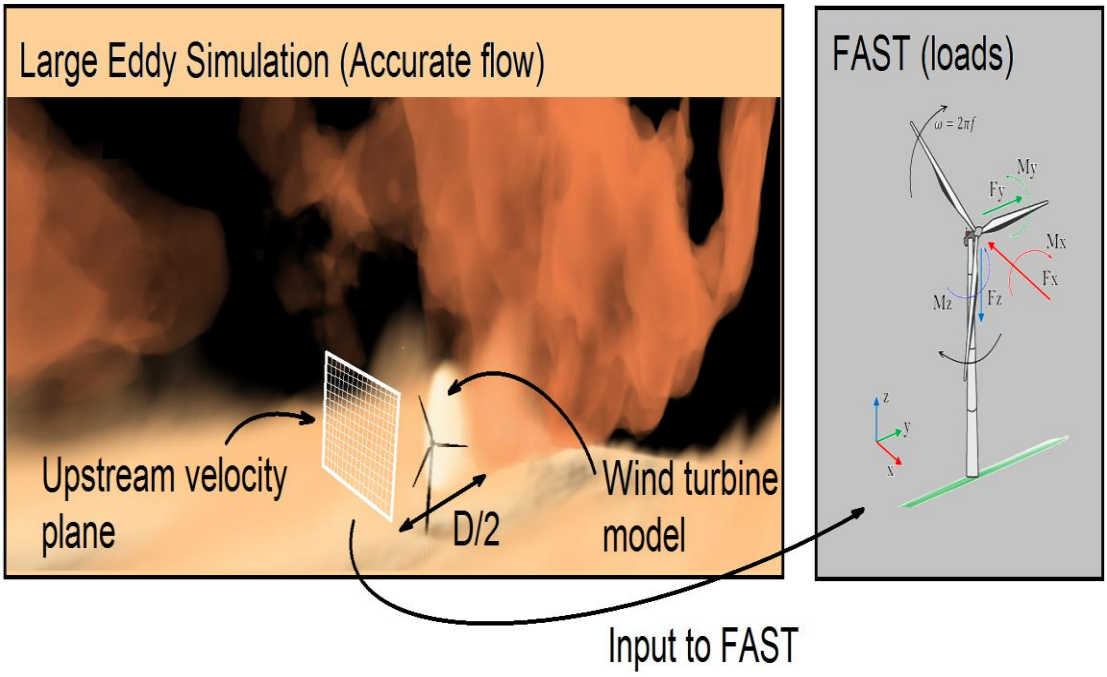

Figure 3.6. Schematic representation of rotor load computation using LES and FAST.

3.4.1. Rotor loads

Rotor loads can be defined as the loads caused by the operation of the wind turbine at the hub of the wind turbine tower. Turbine loads can be further separated into the following categories (*65*)

- Aerodynamic loads from a uniform, steady wind speed generate a stationary load.
- A stationary, but spatially uneven flow field over the swept area causes cyclic load changes on the turning rotor.
- The mass forces that result from the rotating rotor blade weight cause periodic, nonstationary loads.
- In addition to the stationary and cyclic loads, the rotor is exposed to nonperiodic and random loads caused by wind turbulence.

Hence, the wind turbine rotor loads include inertial, gravitational, and aerodynamic forces acting on the rotor combined with acceleration and other dynamic reactions. The primary aim of this work is to study the forces developing on a wind turbine in a streamwise direction. Hence, the out-of plane shear at blade root (RootFxc), the fore-aft thrust force at the hub (Fxt), and the fore-aft bending moment at the hub (Myt) are the rotor loads that will be studied (see Figure 3.7 for a schematic representation of these forces and moments). Figure 3.8 provides a representation of the out-of plane shear at the root of the wind turbine blades (RootFxc). Wind turbine loads are dynamic in nature, hence complex, and in order to accurately compute the rotor loads, a tool developed by the National Renewable Energy Laboratory called FAST is used this study. A detailed description of FAST is presented in the next section.

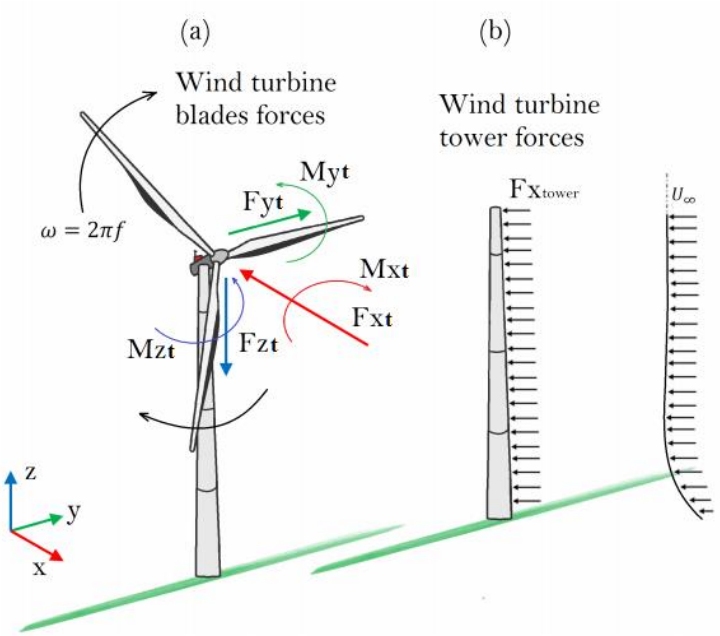

Figure 3.7. Wind turbine rotor loads and tower loads representation.

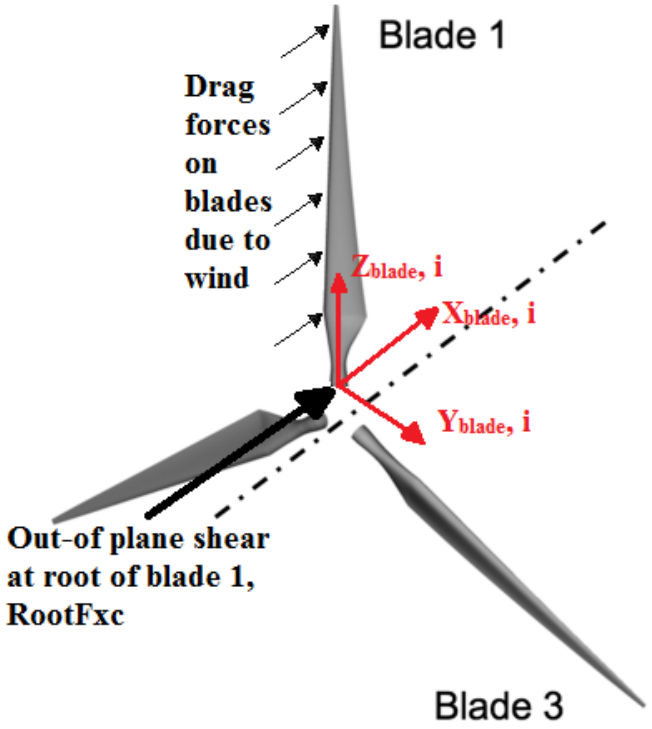

Figure 3.8. Representation of out-of plane shear at the root of blade 1, RootFxc.

3.4.1.1. FAST and NREL 5MW onshore wind turbine

FAST is an aero-elastic simulation code developed by the National Renewable Energy Laboratory, Colorado (*64*) to simulate the coupled dynamic response of wind turbines. The FAST tool enables the analysis of a wide range of wind turbine configurations, including two or three-blade horizontal-axis rotor, pitch or stall regulation, rigid or teetering hub, upwind or downwind rotor, and lattice or tubular tower. The wind turbine can be modeled on land or offshore on fixed-bottom or floating substructures. FAST uses wind-inflow data (in this work provided by the different LES cases) and solves for the rotor-wake effects and blade-element aerodynamic loads, including dynamic stall. The structural-dynamic models apply the control and electrical system reactions, the aerodynamic and hydrodynamic loads, as well as the gravitational loads. It also simulates the elasticity of the rotor, drivetrain, and support structure.

In this study, we are using the 5MW NREL onshore wind turbine as our reference wind turbine model (*66*). It has a rotor diameter of 126 m and a hub-height of 90 m. It uses variable-speed and collective pitch-control configuration with a rated wind speed of 11.4 ms^{-1} and rated rotor speed of 12.1 rpm. The wind turbine has a cut-in velocity of 3 ms^{-1} and a cut-out velocity of 25 ms^{-1}. The wind turbine was modeled using a combined modal and multibody dynamics formulation. The tower is assumed to be fixed rigidly to the ground. The wind turbine is pitch-controlled and the pitch angles in the wind turbine can vary from zero to 23.7 degrees depending upon wind speed. Note that the rotor diameter and hub-height have been set according to the NREL 5MW wind turbine in our LES wind turbine model mentioned in section 3.2. The specifications of the 5MW wind turbine are given in Table 3.1.

Table 3.1. 5 MW NREL onshore wind turbine properties (*66*).

Specifications	**Values**
Power rating	5 MW
Rotor orientation, configuration	Upwind, 3 blades
Control	Variable speed, collective pitch
Rotor, hub diameter	126 m, 3 m
Hub-height	90 m
Cut-in, rated, cut-out wind speed	3 m/s, 11.4 m/s, 25 m/s
Cut-in, rated rotor speed	6.9 rpm, 12.1 rpm
Rated tip speed	80 m/s
Overhang, shaft tilt, precone	5 m ,5^{o}, 2.5^{o}
Rotor mass	110,000 kg
Nacelle mass	240,000 kg
Tower mass	347,460 kg

3.4.2. Tower loads

Wind turbine tower loads (Figure 3.7) are computed using the conventional drag force equation for a cylinder (*32*),

$$F_X = 0.5 C_D \rho {U_h}^2 \pi R \Delta_z$$

where ρ is the density of air , C_D is the drag force coefficient for the cylinder, U_h is the velocity in front of the tower for each grid point, R is the outside radius of the wind turbine tower, and Δ_Z is the grid spacing in Z. In this study, density of air, ρ, is taken equal to 1.255 kg/m^3, the vertical grid spacing (Δ_Z) is constant with a value of 7.8 m (LES vertical resolution), and the drag force coefficient C_D is taken as 1. The value of the drag coefficient depends on the Reynolds' number, which in our case varies from 10^6 to $4x10^6$ depending on the velocity. A value of 1, which is slightly on the higher end, was selected based on the drag coefficient graph for increasing Reynold's number (see Figure 3.9).

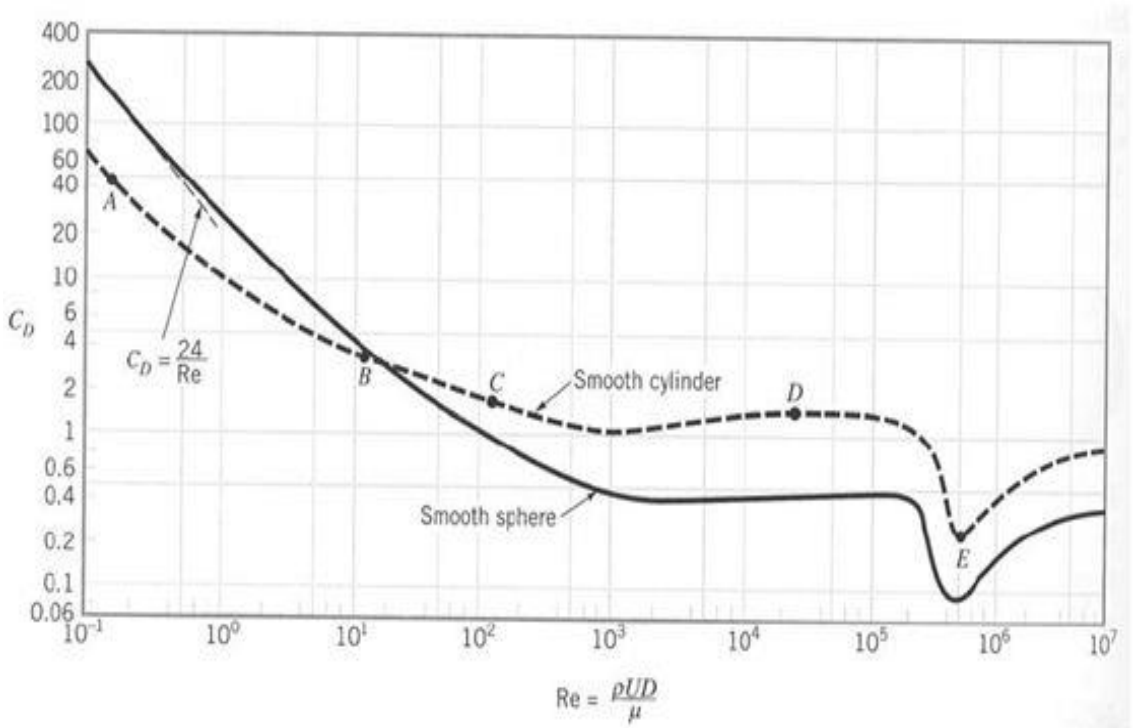

Figure 3.9. Drag coefficient for cylinder for different Reynold' numbers.

3.5. Shear force and bending moment along the wind turbine tower height

Shear forces and bending moments are computed for all the different cases along the wind turbine tower height in the streamwise direction. Rotor thrust, Fxt, fore-aft bending moment at tower top, Myt, and tower forces due to wind, Fx, are used in the computation of the shear force and bending moment. Figure 3.10 shows a nodal representation of a typical wind turbine tower.

Shear force (S.F) at a given node, n is computed using,

$$S.F = Fxt + \sum_{i=1}^{n} Fxi$$

Bending moment (B.M) at a given node, n is computed using,

$$B.M = Myt + Fxt * (n-1)dz + \sum_{i=1}^{n} Fxi * (n-i)dz$$

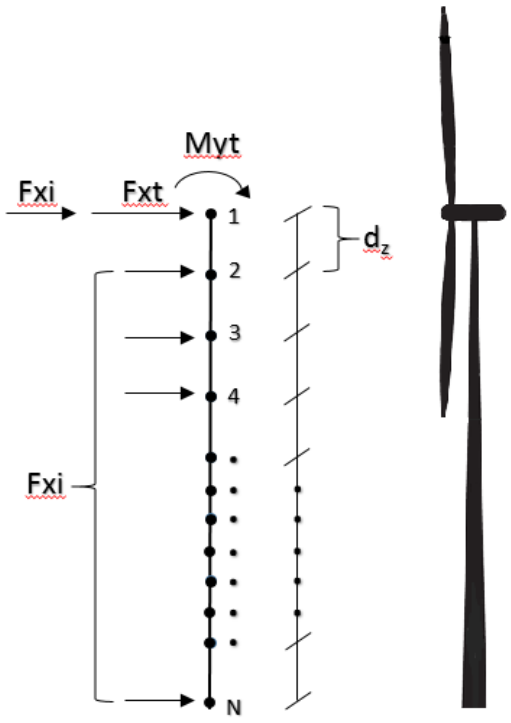

Figure 3.10. Nodal representation of wind turbine tower for S.F/B/M computation.

where, n = node where S.F/B.M is to be computed,

i = node number,

dz = grid spacing in Z direction,

N = total number of nodes,

Fxi = tower force at node i,

Fxt = rotor thrust force,

Myt = fore-aft bending moment at top of the tower.

CHAPTER 4

STUDY CASES

4.1 Large eddy simulation configuration

The LES study cases were developed for a total of 48 hours (real time), replicating a realistic evolution of an atmospheric flow for a period of two complete days. The domain size was set to ($\pi \times \pi \times 3$) z_i, where z_i is the height of the boundary layer, initially located at 1000 m height. A fairly high numerical resolution was used (Δ_X, Δ_Y = 24.5 m and Δ_Z = 7.8 m), with a computational domain of 128 × 128 × 384 grid points. The numerical simulations were forced with a height-independent and time-constant geostrophic wind of value (u_G, v_G) = (9, −3) ms^{-1} together with a time-varying surface temperature, hence replicating a realistic diurnal flow. The simulations were initialized with a height-independent geostrophic wind, and a well-mixed temperature profile matching the initial surface temperature of 278.6K, with an inversion layer spanning from z_i to the top of the domain. The LES was initialized with vertical profiles of velocity and temperature extracted from Kumar et al. (*67*). Shown in Figure 4.1 is the surface temperature imposed as bottom boundary condition, which reproduces a realistic change of temperature during two consecutive diurnal cycles. A separate simulation was performed for the neutral boundary layer (NBL) case, with the same geostrophic wind forcing but with a constant temperature profile capped by an inversion layer at the top of the ABL.

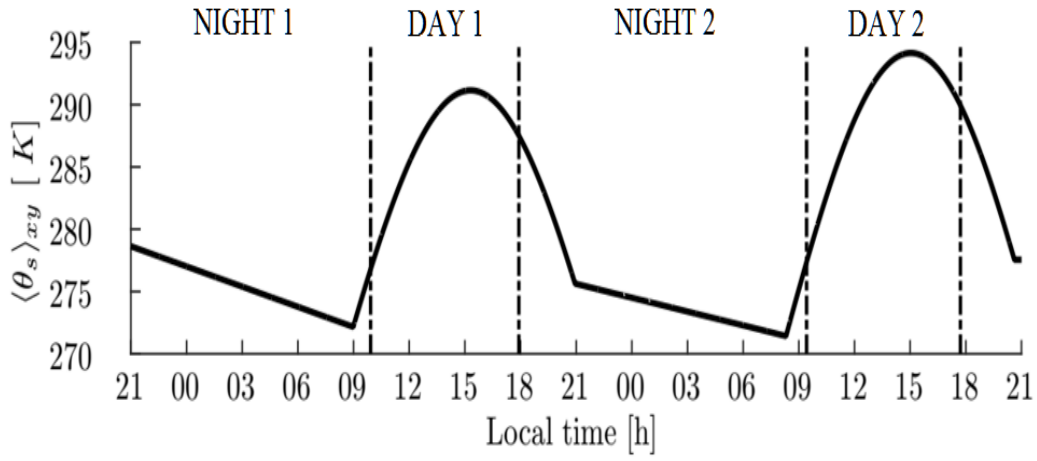

Figure 4.1. Temperature profile used in LES (diurnal cycle).

4.1.1. In-plane velocity

The three components of the in-plane velocities (u, v, and w) are extracted D/2 upstream (where D is the rotor diameter) of the wind turbine using the characteristic box realigned flow. The plane is 156 m x 156 m in the spanwise (Y) and vertical (Z) directions, respectively, with a total of 40 grid points in each direction. In the transformation of reference frame from the LES to the flow-aligned turbine box, the flow is linearly interpolated and mapped to a finer numerical resolution grid (Dx_{box} = Dy_{box} = 3.9 m). In-plane velocities with a time-step of 0.2 seconds are extracted for a total duration of 60 minutes (seen later in section 4.2). Hence, an in-plane velocity plane for a single wind turbine consists of 40 x 40 x 18000 velocity points. This 3D wind field is fed into FAST to compute the corresponding rotor loads. Figure 4.2 shows the upstream location of the velocity plane along with the Y and Z dimensions of the plane.

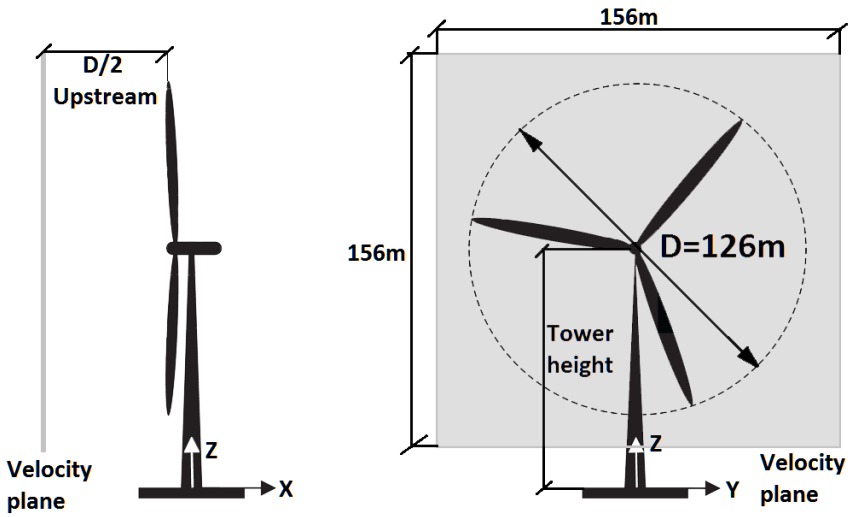

Figure 4.2. YZ velocity plane representation used as input to compute rotor loads using FAST.

4.2. Atmospheric Stratifications

The three characteristic atmospheric stratification states experienced throughout a characteristic diurnal cycle (see Chapter 2), unstable (CBL), neutral (NBL), and stable (SBL) are studied in detail in this work. Each stratification case was studied for periods of 60 minutes (see Figure 4.3). These periods, while short, are representative of the flow during the stable, unstable, and neutral stratification and avoid the continuous non-stationarity intrinsic to any diurnal cycle.

4.3. Wind turbine configurations

Two different wind turbine configurations, the single wind turbine and a wind farm, are considered. These are the most representative cases of currently installed wind turbines.

4.3.1. Wind farm (WF)

The wind farm configuration consists of 24 wind turbines distributed in 4 rows and 6 columns. The spacing in the streamwise direction (S_X) is 7D and in the Y direction (S_Y) is 5D, where D is the rotor diameter (Figure 4.4). As a result of the periodicity of the

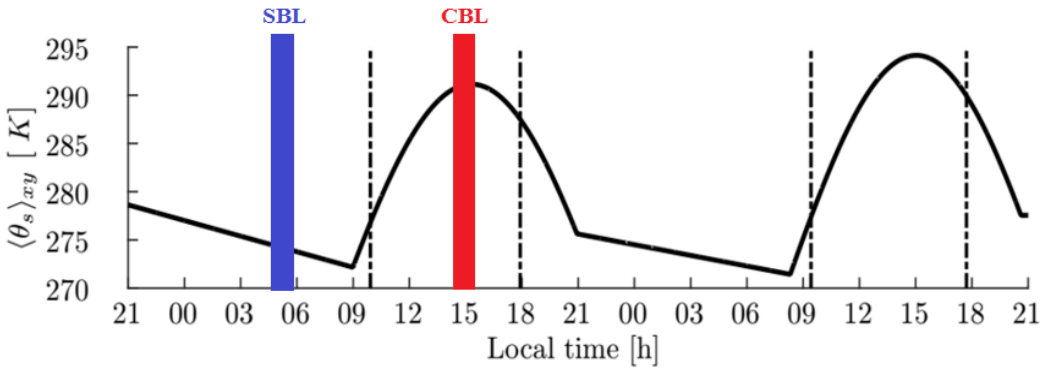

Figure 4.3. Convective and stable boundary layer regions in the diurnal cycle used in the research.

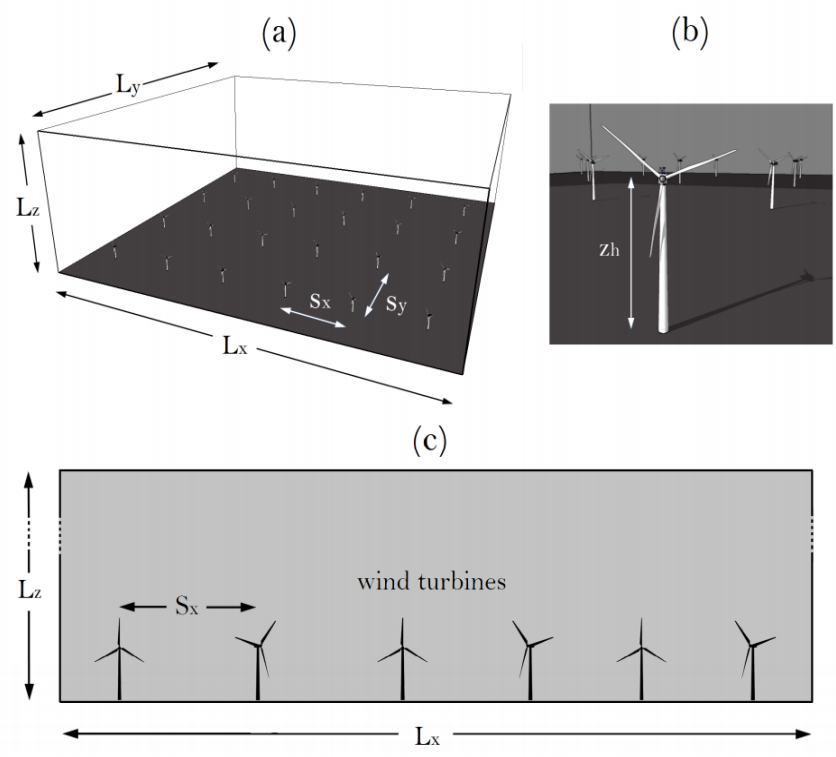

Figure 4.4. Wind turbines in LES (a) Wind farm configuration in the LES domain. (b) Typical wind turbine in a wind farm, z_h is the hub-height. (c) Wind turbines yaw aligned randomly according to the direction of wind flow.

numerical domain, this wind farm is in practice infinite in extension, also so-called a very-large wind farm. The wind turbine model readjusts the yaw orientation every 10 minutes according to the averaged wind vector measured at the predetermined upstream scanning distance (*53*) and hence, wind turbines in the farm can be oriented in any random direction, adjusting to the incoming wind vector (Figure 4.4 c).

4.3.2. Single wind turbine (SWT)

The SWT configuration consists of a wind turbine placed in isolation, or a wind farm where the constituent wind turbines are highly spaced (with S_X = 63 D and S_Y = 31D) and hence do not interact with each other (see Figure 4.5). For this case, the characteristics of the wind turbine are exactly the same as the ones described in the WF case.

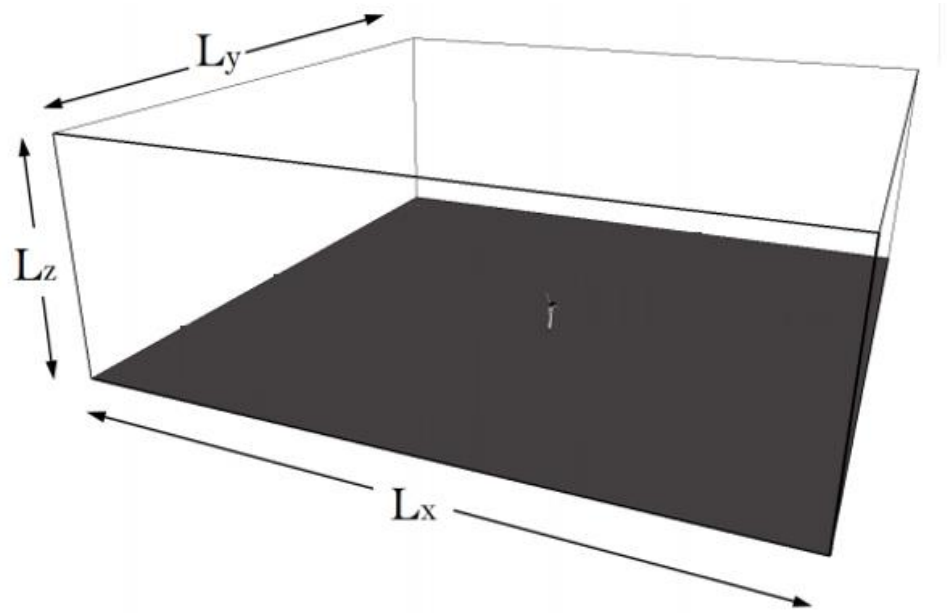

Figure 4.5 Single wind turbine configuration in the LES domain.

4.4. Tower heights

The tower height, $z_{h,}$ varies between 90 m and 150 m, keeping the rotor diameter constant at D = 126 m, equal to the 5MW NREL's onshore wind turbine. In simple terms, it means that the wind turbine blades are shifted higher with the help of a taller tower. Figure 4.6 represents the different heights of wind turbines used in this study. The tower dimensions for the 90 m wind turbine tower (see Table 4.1) are adapted from the NREL's 5MW baseline onshore wind turbine (*66*). For wind turbines of height 100 m -150 m, the same external diameters have been used in the study. Note that the wind-induced tower forces only depend on the frontal area of the wind turbine tower, and thus tower dimensions would increase with the increase in height and so would the tower forces. However, this increase would be very small when compared to the rotor thrust, Fxt, hence a top diameter of 3.87 m and base diameter of 6 m have been used for all tower heights to compute the tower loads.

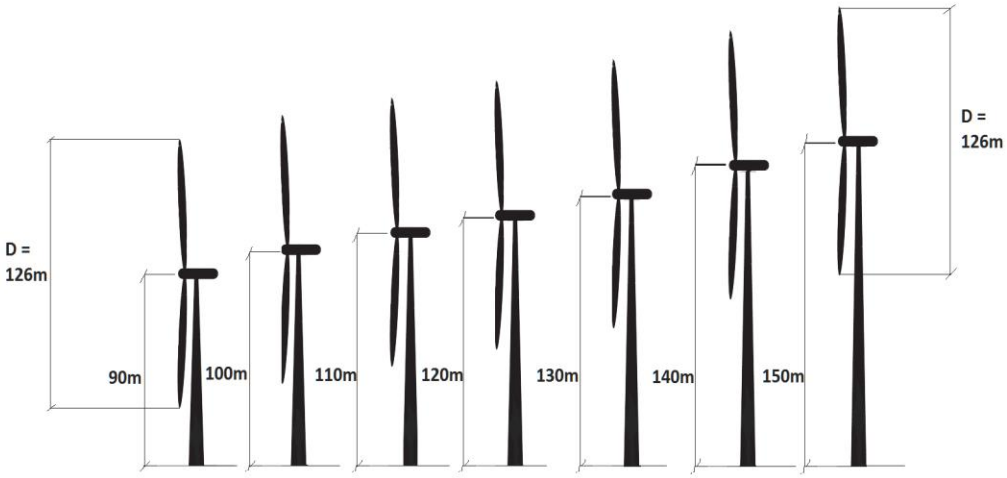

Figure 4.6. Varying tower heights from 90 m – 150 m used in the study.

Table 4.1. 5MW NREL onshore wind turbine tower dimensions (*66*).

Property	**5 MW NREL onshore wind turbine**
Tower height	90 m
Base diameter	6 m
Base thickness	0.035 m
Top diameter	3.87 m
Top thickness	0.025 m

4.5. Summary of study cases and framework to compute the results

Figure 4.7 shows a summary of the different cases studied in this project, and Figure 4.8 shows the framework used to compute the results. In summary, large eddy simulations were performed for the single wind turbine and wind farm cases in a diurnal cycle for seven increasing heights, resulting in a total of 14 LES simulations. Using the characteristic box tool, a flow field of u, v, and w velocities in a YZ plane, -D/2 upstream of the wind turbine are obtained for the convective, neutral, and stable boundary layers, respectively, for each case. Hence, a total of 42 velocity planes are obtained in the study. For each boundary layer, 60-minute time-series data of velocities are obtained with a frequency of 5 Hz (Time step of 0.2s). The velocity plane size is 156 m x 156 m and has a resolution of 3.9 m. This wind field is then postprocessed into a file format suitable for input to FAST

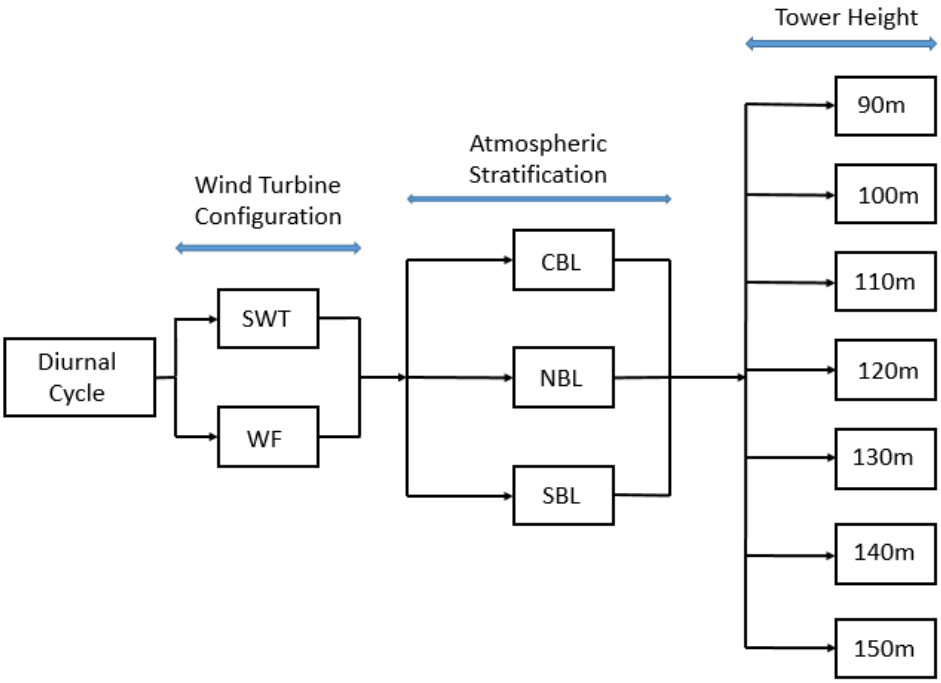

Figure 4.7. Summary of the different study cases in the study.

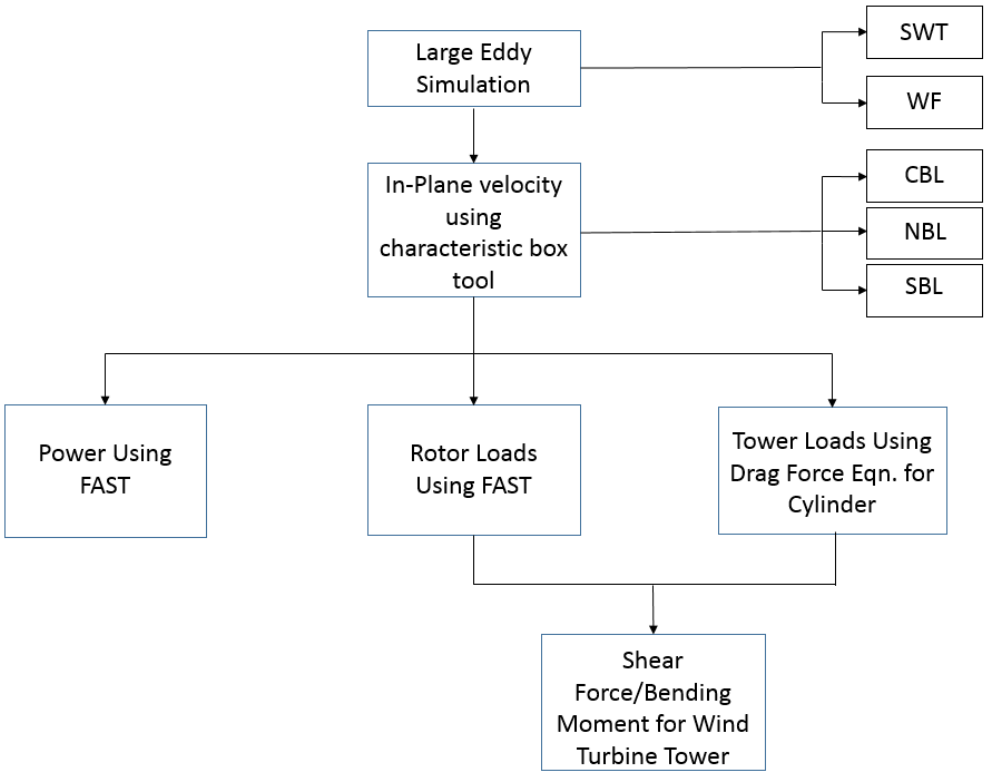

Figure 4.8. Research study framework.

using our in-house MATLAB conversion code. The rotor loads are then computed using FAST for the 5 MW NREL baseline onshore wind turbine for all the different cases. Note that FAST does not feed information backwards into the LES code. The tower loads are obtained using the conventional drag force equation mentioned in section 3.4.2. With a combination of rotor and tower loads, we also compute the shear force and bending moment distribution along the height of the wind turbine tower. Along with the loads, the streamwise hub-height velocity, the rotor rotational speed, and the power output are also computed.

CHAPTER 5

RESULTS

Within this chapter, a detailed analysis of the major forces arising on the wind turbine will be provided. Precisely, this chapter will characterize forces acting in the streamwise direction, the out-of plane shear force at the blade root, the fore-aft shear force at the hub, and the fore-aft bending moment at the hub. To better understand these results, data corresponding to the streamwise hub-height velocity, the turbulence intensity, the rotor rotational speed, and the power output will also be provided.

5.1. Hub-height streamwise velocity

In order to understand the differences in the flow field encountered in the different wind turbine configurations under different atmospheric stratifications, a vertical section of the streamwise velocity for the 90 m wind turbine is shown in Figure 5.1. These vertical slices of the LES domain help us understand the structure of the streamwise velocity field around the wind turbine for the different study cases. The subplots on the left represent the SWT cases and those on the right column represent the WF case. It can be observed that higher velocities are observed for the SWT case in comparison to the WF case. For those turbines placed within a large wind farm, a reduced velocity is measured upstream of the rotor disk as a result of the wakes of the upstream wind turbines. For the SWT case, during

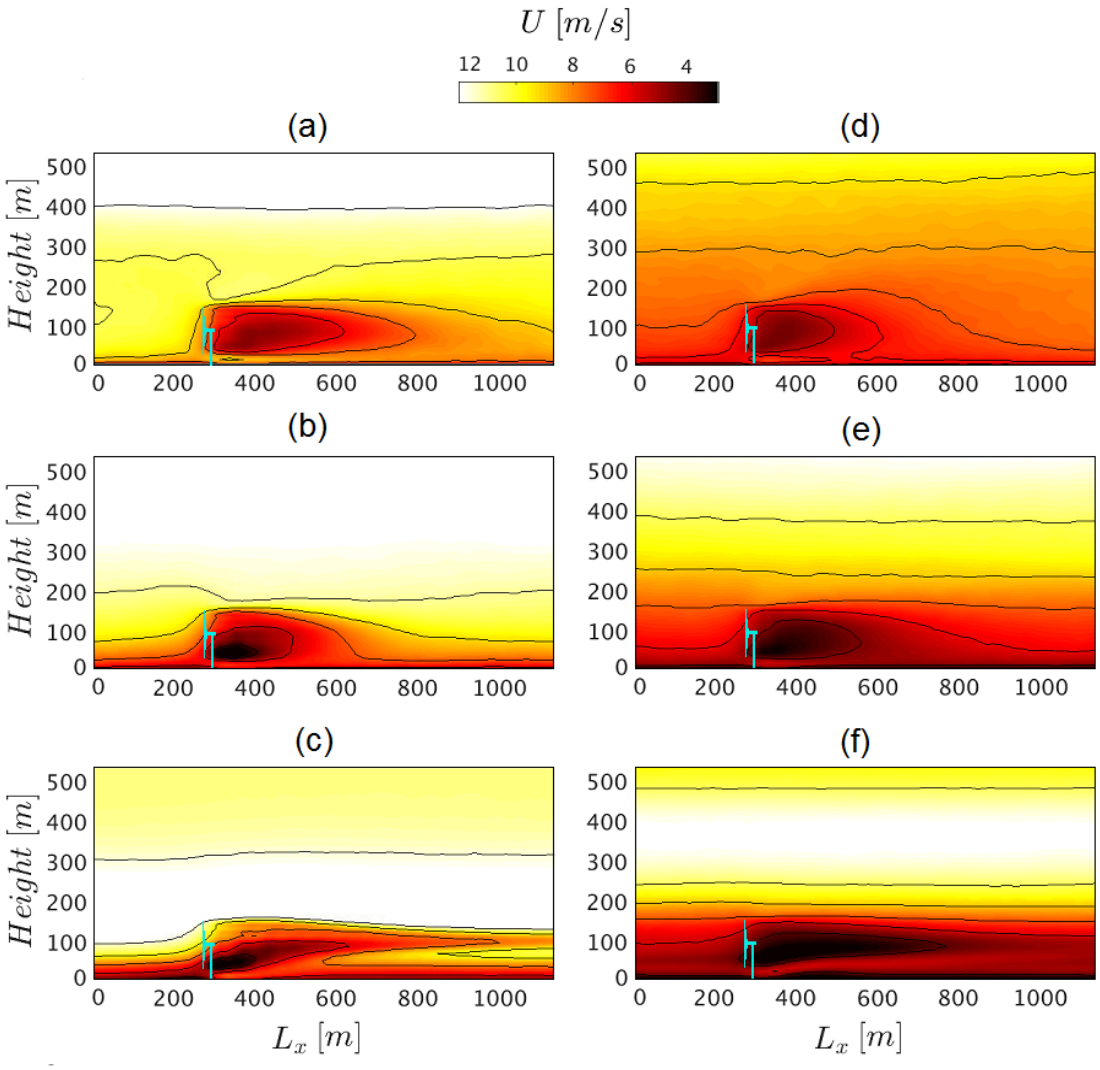

Figure 5.1. Vertical section of streamwise velocity, U through the LES wind field for 90 m wind turbine for (a) SWT CBL (b) SWT NBL (c) SWT SBL (d) WF CBL (e) WF NBL (f) WF SBL cases.

CBL conditions (subplot a), a reduction in velocity is observed from the surface to around 400 m. A similar reduced velocity region is observed for the WF case under the same stratification conditions (subplot d), but in this case ranging from the surface up to around 600 m. Wind speeds increase gradually for both the SWT and the WF cases under the neutral boundary layer (subplot b and e). An important aspect of the SBL stratification is the occurrence of a higher band of velocity, known as the low-level jet (LLJ), observed at heights varying from 100 to 500 m (*51*). In our study, the LLJ is observed during stable conditions for a single wind turbine at around 150-300 m (as seen in subplot c) and at around 600 m for the wind farm case (subplot f). For the 90 m wind turbine, the LLJ is observed near the top of blades shifted slightly upwards due to the effect of the rotor. This is, however, not seen for the WF case during night time, where the LLJ is shifted above the turbines as a result of the much enhanced friction induced by the large amount of turbines conforming a large wind farm. The SWT case under SBL conditions is further explored because of the relevance and peculiarity of the LLJ feature. In this regard, Figure 5.2 also illustrates vertical slices of the average streamwise velocity field for the 150 m hub-height turbine. Both cases show good similarities and the LLJ is observed for the 150 m turbine as well. It is interesting to note, however, that for the taller wind turbine, there exists a reacceleration of the flow under the rotor disk, not observed for the 90 m hub-height turbine. Both the effect of this LLJ and the reacceleration below the rotor disk, will later be shown to affect the wind turbine loads. Figure 5.3 shows time averaged (60-minutes) vertical profiles of the streamwise velocity measured D/2 upstream of the turbine's rotor disk, for all seven wind turbine heights, under different stratifications, and wind turbine configurations. To be able to represent such amount of data in a compact form, the figure

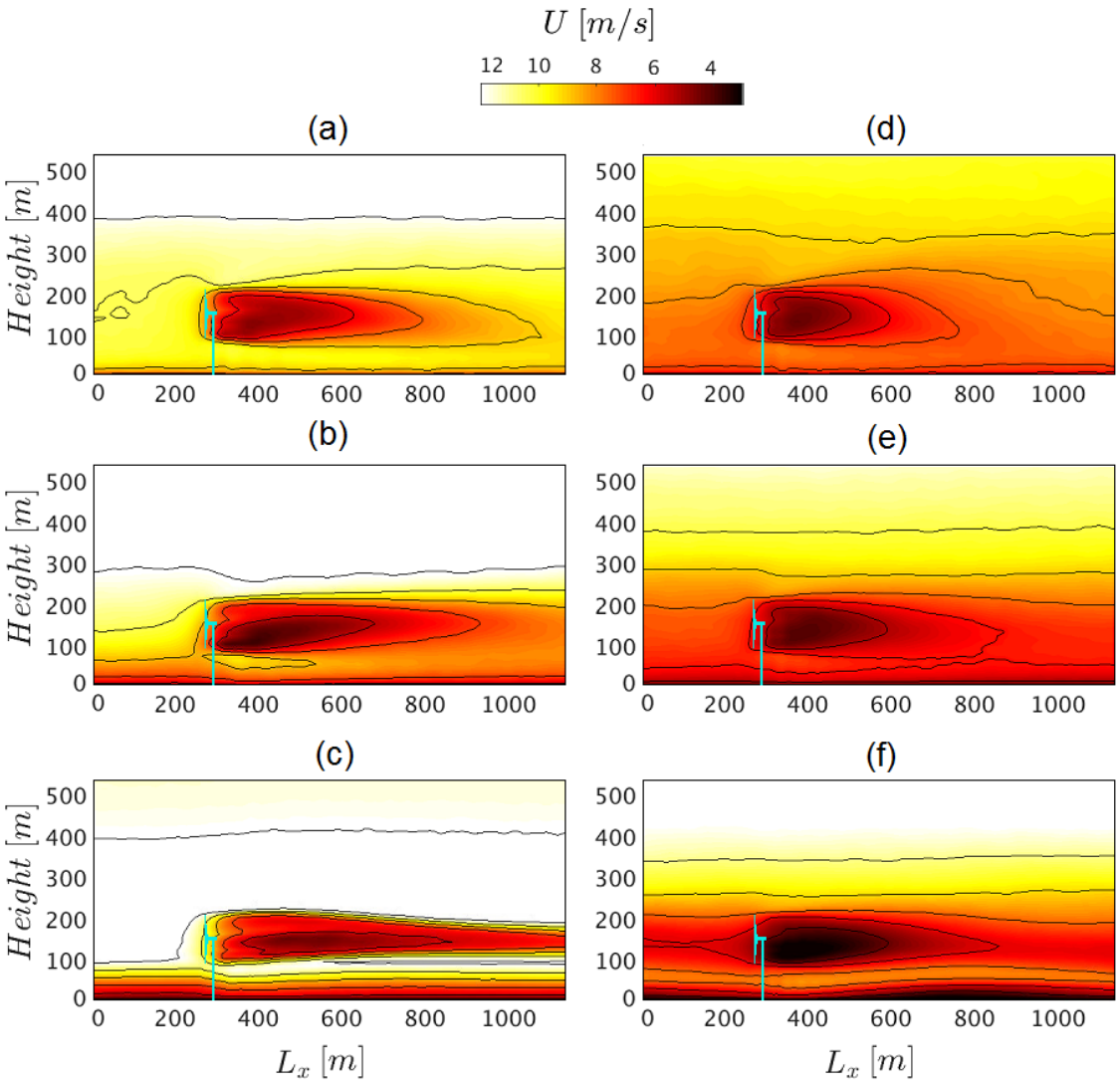

Figure 5.2. Vertical section of streamwise velocity, U through the LES wind field for 150 m wind turbine for (a) SWT CBL (b) SWT NBL (c) SWT SBL (d) WF CBL (e) WF NBL (f) WF SBL cases.

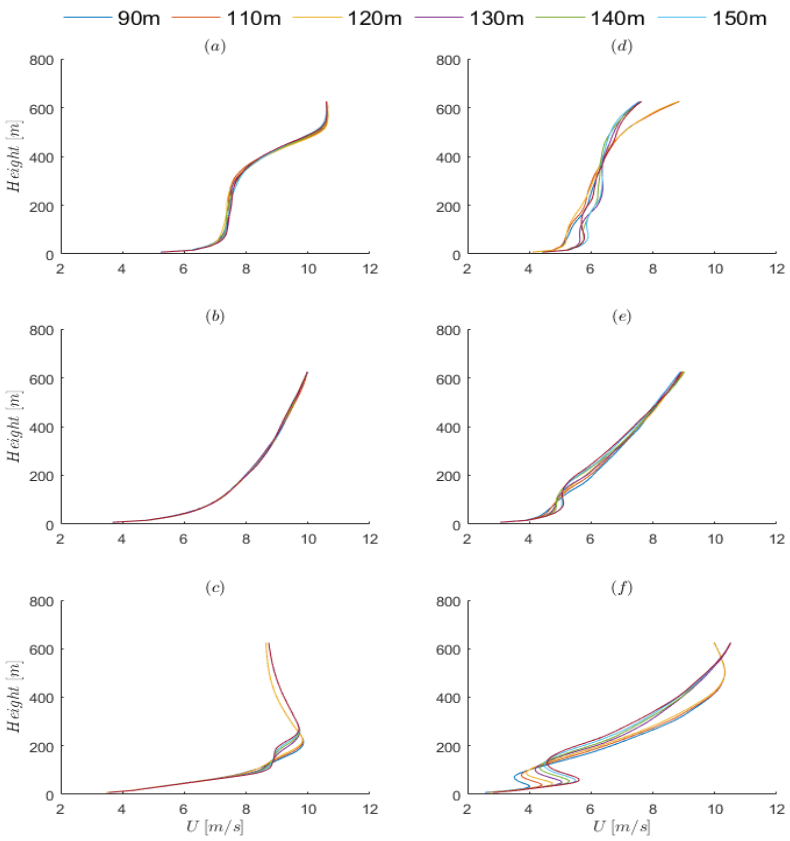

Figure 5.3. Vertical wind profile for streamwise velocity, U for (a) SWT CBL (b) SWT NBL (c) SWT SBL (d) WF CBL (e) WF NBL (f) WF SBL cases.

is structured such that the left column represents results for the SWT case and right column represent the WF case. Also, each row represents a different atmospheric stratification case; from top to bottom are the CBL, the NBL, and the SBL cases, respectively. Within each subplot, the different turbine hub-heights are correspondingly further differentiated. This figure structure will be consistently used throughout this chapter. Further, for shorter reference a single wind turbine with 90 m tower height will be denoted as SWT90 and the corresponding wind farm case as WF90.

In Figure 5.3, it can be seen that for the SWT case under CBL conditions (subplot a) the wind profile increases in an interesting pattern, with a strong wind shear near the surface

and above 300 m, while a nearly vertical profile is observed between 70 m and 300 m height. This is the result of the strong convective mixing. For the WF-CBL case (subplot d), the wind shear slope is on average constant, with some minor fluctuations above the turbine's rotor disk. For the SWT under NBL conditions (subplot b), the wind profile is almost identical to the one obtained using the traditional IEC 61400-1 design guidelines power law. A similar profile is observed for the WF neutral case (subplot e), but with a more noticeable impact induced by the top of the turbine's rotor. In contrast, the SBL stratification presents very distinctive characteristics for both cases. For the SWT, there exists a strong vertical wind shear, up to the "nose" of the LLJ, which is observed at around 180 to 200 m, depending on the turbine case. At this height, the wind is super-geostrophic with a mean velocity of 10 ms^{-1}. For wind turbine heights between 90 m and 120 m height, the LLJ always impinges on the top most part of the turbine's rotor. However, for those higher turbines (cases of 130 m, 140 m, and 150 m), the LLJ directly impinges the rotor disk, diverging into two high-speed bands, above and below the turbine's rotor disk (subplot c). For the WF case, strong wind shear is observed below and above the rotor area. Due to the reduced convective mixing at night, wind speed increases quickly up to the bottom of the blades, where a reduction in velocity is observed due to the wake effect of the upstream wind turbines. After crossing the top rotor blades, the velocity increases rapidly until a height of around 600 m, where it forms the low-level jet.

To better evaluate the differences in mean velocity as a function of turbine hub-height, Figure 5.4 shows a box-plot representation of the streamwise hub-height velocity for all the different study cases. During the CBL and NBL conditions, for both the SWT and WF cases, the velocity mean values do not change considerably with increasing turbine height

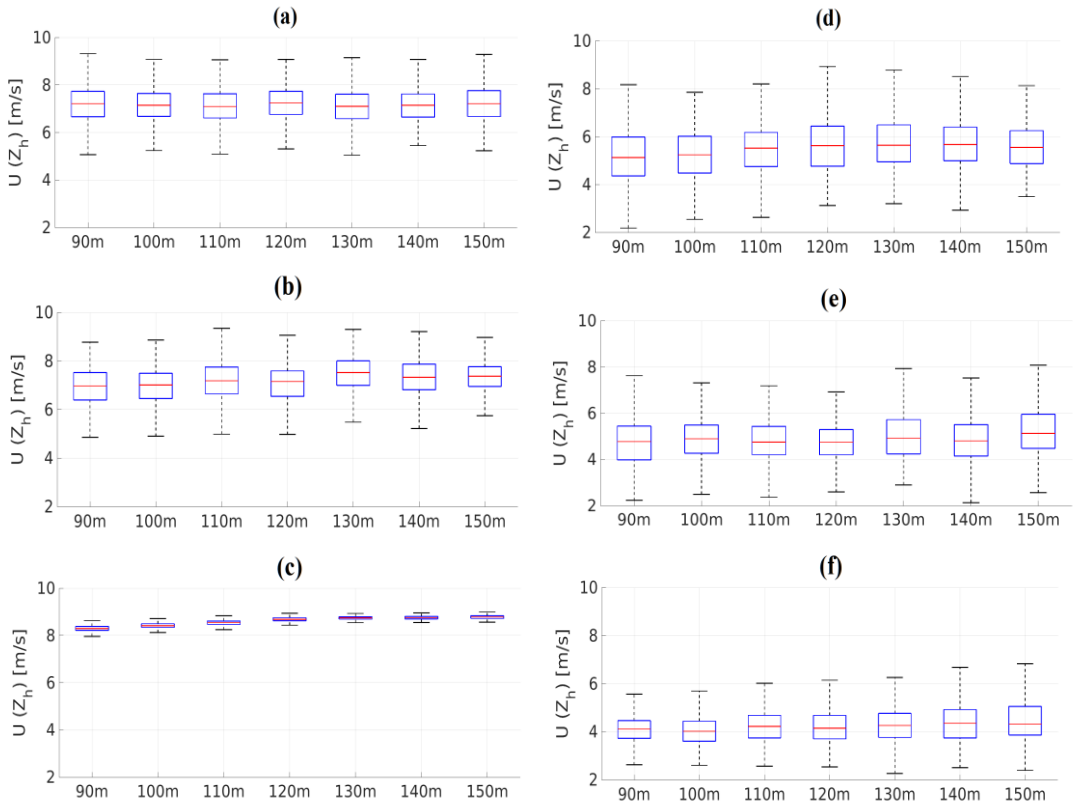

Figure 5.4. Box-plot representation of hub-height velocity, U for increasing tower height for (a) SWT CBL (b) SWT NBL (c) SWT SBL (d) WF CBL (e) WF NBL (f) WF SBL cases.

(subplots a, b, d, and e). The mean velocity for the SWT is approximately 7.5 ms^{-1} with a standard deviation of 2 ms^{-1} and for the WF case, the mean velocity is nearly 5.5 ms^{-1} with a standard deviation of approximately 3 ms^{-1} for the seven different turbine heights. On the contrary, during the SBL period, interesting results are observed for both the SWT and the WF cases (subplots c and f). For the SWT, the mean velocity values increase from 8.3 ms^{-1} for the 90 m turbine to 8.8 ms^{-1} for a 150 m tower (6% increase), and the velocity standard deviation decreases from 0.5 ms^{-1} to 0.3 ms^{-1} (40% decrease), indicative of smoother flows as a function of height. For the WF case under SBL, the mean velocity values also increase, in this case from 4.1 ms^{-1} to 4.4 ms^{-1} (7% increase) between the 90 m and 150 m height

turbine. On the contrary, in this case, the standard deviation also increases from 1.7 ms^{-1} for the 90 m turbine to 2 ms^{-1} for the 150 m turbine (18% increase). This increase in the mean velocity standard deviation as a function of height is believed to be induced due to the increased spacing between the ground and the bottom of the blades, leading to entrainment of air, which enhances mixing and thereby increases turbulence.

5.2. Turbulence intensity

To better understand the results shown for the streamwise velocity in section 5.1, turbulence intensity is investigated next. Turbulence intensity is a measure of flow turbulence, expressed as a percentage with respect to the mean velocity, hence

$$T.I = \frac{\sqrt{\overline{u'u'}}}{U}$$

In this case, $\sqrt{\overline{u'u'}}$ is the root-mean-square-of the turbulent velocity fluctuations and U is the mean hub streamwise velocity. Shown in Figure 5.5 are the corresponding box-plots for all the different study cases. It can be observed that the mean TI values for the WF cases are in general two times larger than those observed for the SWT cases. The turbulence intensity values during the CBL and NBL conditions for the SWT case (subplots a and b) are close to 8% and for the WF case about 15%, almost doubling the turbulence intensity values of the SWT case. This is a remarkable result indicative that the fluctuating loads encountered for a turbine within a large wind farm could be more severe than when installed isolated from other turbine. For the stable conditions interestingly, TI decreases to 2% for the SWT case and to 10% for the WF case (almost a 5-fold the TI observed for a SWT under the same stratification). This increase in turbulence intensity is the result of

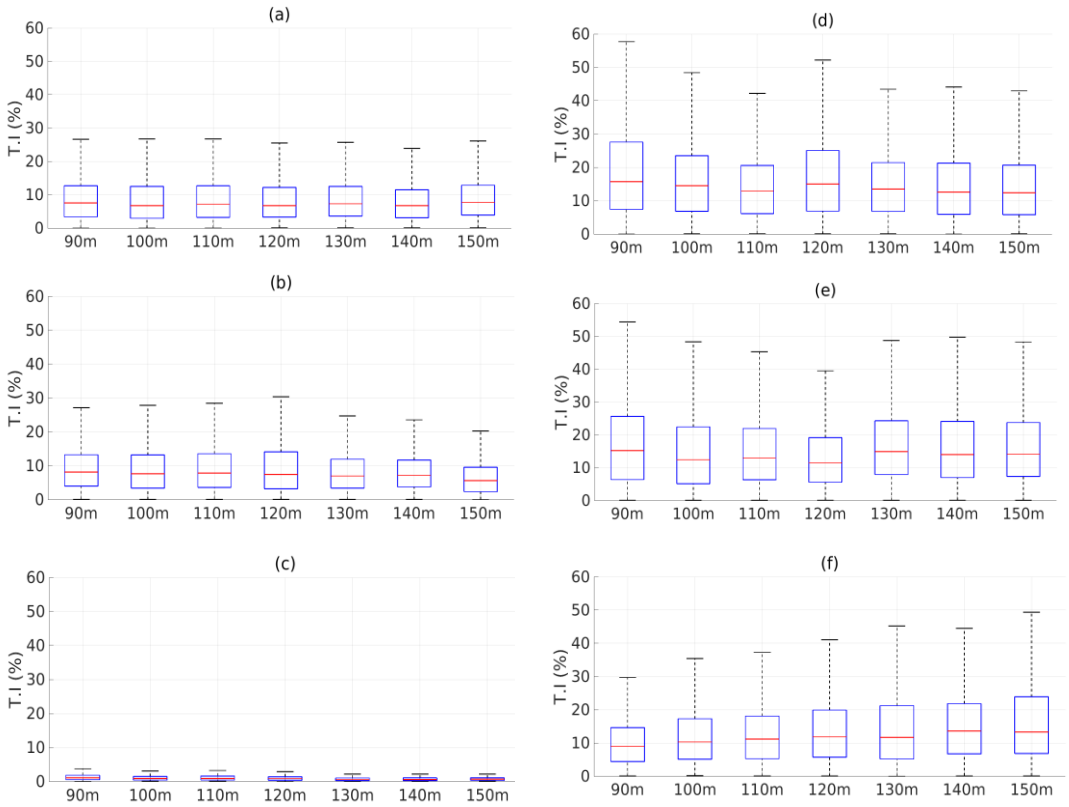

Figure 5.5. Box-plots representation for turbulence intensity, T.I for increasing tower heights for (a) SWT CBL (b) SWT NBL (c) SWT SBL (d) WF CBL (e) WF NBL (f) WF SBL cases.

the continuous wake-to-wake interaction when turbines are placed in close proximity. It is also interesting to note that this enhanced turbulence intensity remains present regardless of the atmospheric stratification, and the difference between the SWT and WF cases is accentuated during night time. It is also interesting to note the decrease in TI for the SWT under SBL conditions (subplot c) with increasing turbine height. A decrease from 2% to 0.75% is observed, indicative of the progressive turbulence attenuation with height. An exactly opposite behavior is observed in the WF case under SBL conditions (subplot f), where the TI increases from 10 % to 16 %. This increase with height, while a-priory counter-intuitive, is believed to be the result of the enhanced mixing present in large wind

farms. An increase in turbulence intensity translates to larger fluctuations in harvested power and increases in fatigue on the turbine's structure.

5.3. Rotor rotational speed

The rated velocity and rated rotational speed for the 5MW NREL wind turbine used in our study are 11.4 ms^{-1} and 12.1 rpm, respectively. When the velocity exceeds the rated value, the loads might increase drastically on the wind turbine, which may lead to the failure of the turbine. In order to prevent this, when the velocity of the wind exceeds 11.4 ms^{-1}, the wind turbines adjust the pitch of their blades, reducing the drag forces on the blades and thus reducing the overall loads on the wind turbine. The wind velocities in our simulation range from 2 to 9 ms^{-1} and hence, the frequency of rotation for each blade will always be less than the rated frequency of 0.2 Hz.

Figure 5.6 (a) and (b) show a general representation of the azimuth angle denoted by

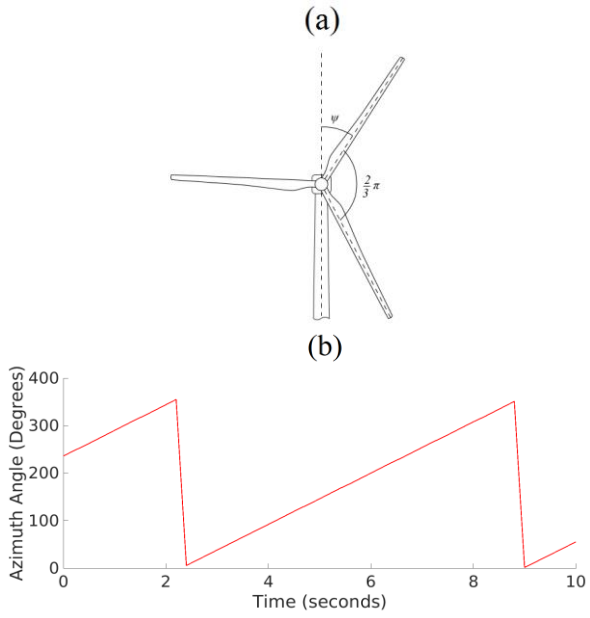

Figure 5.6. Azimuth angle in wind turbines (a) Azimuth angle representation for a 3-bladed horizontal axis wind turbine, (b) Azimuth angle time-series for first 10 seconds of time-series data (CBL S90).

'ψ' and the variation of the azimuth angle for the first 10 seconds of the CBLSWT90 case, respectively. From the figure it can be observed that for a complete cycle, the blades take little more than 6 seconds, indicating that the rotor rotational speed is around 9 rpm. Figure 5.7 shows the corresponding box-plots for the rotational speed. The rotor rotational speed for convective and neutral conditions for the SWT case (Figure 5.7 a, b, d, e) is almost constant at around 8.5 rpm and for a wind farm is around 7.5 rpm. The fluctuations in the rotor speed during convective stability for both the SWT and WF cases are identical at around 2 rpm for all different heights. The fluctuations in the rotor speed in the rotor speed during convective stability for both the SWT and the WF cases are decreased for the neutral stability for both the SWT and the WF cases, and it is around 1.5 rpm. For the stable

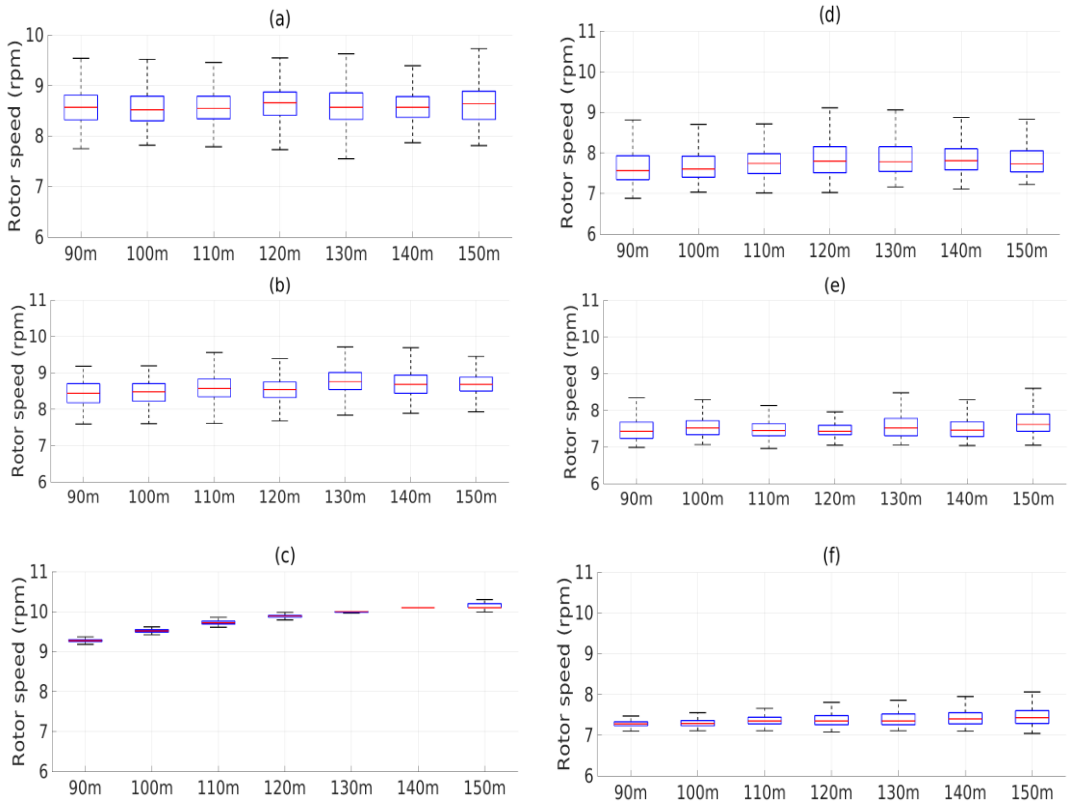

Figure 5.7. Box-plots for rotor rotational speed for all tower heights for cases (a) SWT CBL (b) SWT NBL (c) SWT SBL (d) WF CBL (e) WF NBL (f) WF SBL.

conditions, the single wind turbine shows an almost linearly increasing trend for the rotational speeds. The rotational speed increase from 9.3 rpm for a 90 m WT to 10.15 rpm for a 150 m WT (subplot c). The wind farm during night time, however, shows a marginal increase of rotational speed, from 7.3 rpm for a 90 m WT to 7.45 rpm for a 150 m WT (subplot f). A gradual increase in the standard deviation is observed during this period for increasing wind turbine tower heights.

To provide further insight, Figure 5.8 illustrates the power spectral densities for the rotor rotational velocity. With the help of the PSDs, it is possible to unravel the dominant frequencies that intervene in the rotor rotational velocity. Figure 5.8 shows the power spectral densities for the azimuth angle (rotation of blades) for both the wind turbine configurations and the three atmospheric stratifications for a 90 m wind turbine. It can be observed that the maximum peak occurs at around 0.12-0.16 Hz, followed by consecutive smaller peaks at 2 and 3 times this frequency. The peaks hence appear to be in harmonics of 1P, 2P, 3P, and so on, which are generated by the blade passing through the wind field. The results are consistent since the rotational speed varies from 7 to 9.5 rpm, depending on the WT configuration, boundary layer, and tower heights. The rotational frequencies for a SWT in CBL and NBL conditions (Figure 5.8, a) have peaks at 0.12 Hz, whereas the SWT in SBL presents a slight shift of the peaks towards 0.16 Hz, due to the increased rotational speed. For the WF, since there is not a significant difference between the rotational speeds between the different stability regime, the frequency peaks perfectly overlap (Figure 5.8, b). The wind field and the rotation of the blades are two very important parameters understanding the loads and power production of the wind turbine and hence, their corresponding influence on the wind turbine loads will be discussed next.

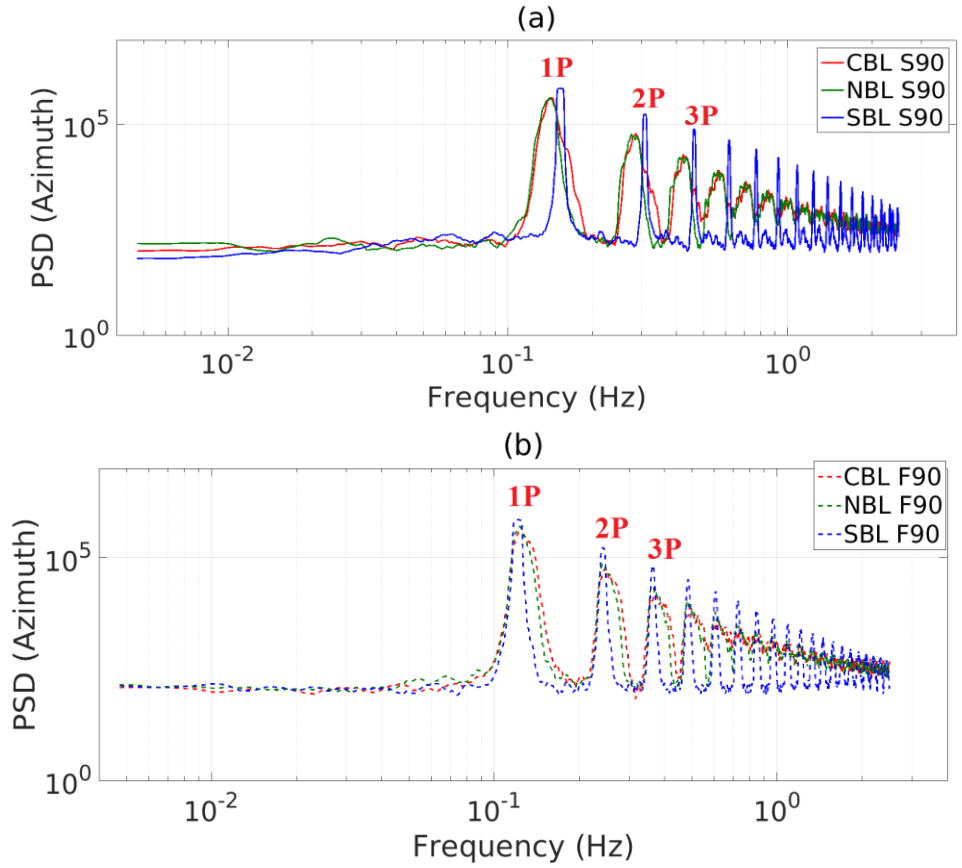

Figure 5.8. Power spectral density of the azimuth angle/rotation of the blades for (a) S90 (b) F90 cases.

5.4. Out-of plane shear at blade root, RootFxc

Out-of plane shear at blade root (RootFxc) is the force acting at the root of a single blade in the direction of the flow, resultant of the aerodynamic wind loads (see section 3.4.1). The RootFxc acts on the rotating frame of the turbine rotor (see Figure 3.7) and represents the force for each individual blade.

From Figure 5.9, it can be observed that for a SWT and under CBL and NBL conditions, the RootFxc remains almost constant with a value of 135 KN, regardless of the turbine heights (subplots a and b). A similar constancy pattern is observed for the WF case under the same stratification conditions, in this case, the approximate constant value for

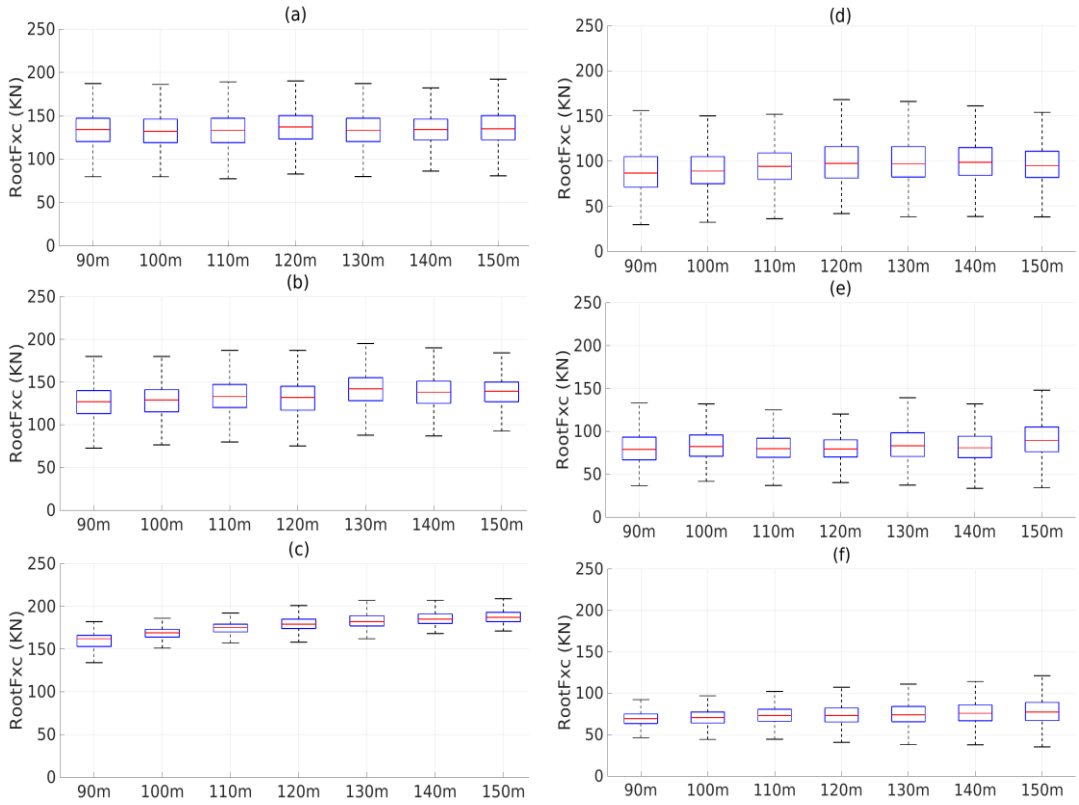

Figure 5.9. Box-plots for out-of plane shear at blade root, RootFxc, for all tower heights for cases (a) SWT CBL (b) SWT NBL (c) SWT SBL (d) WF CBL (e) WF NBL (f) WF SBL.

the same stratification conditions. In this case, the approximate constant value for the RootFxc is of 90 KN (subplot d and e). In the case of a SWT under SBL conditions, results show an increase in RootFxc from 158 KN at 90 m to 188 KN at 150 m (subplot c). This increase with height is almost linear and represents a total increase of 20% between both extreme cases. An increase of 10% is also observed for the case of a WF under SBL conditions; however, this increase is accompanied with an increase in the standard deviation of RootFxc from 8% to 13%. This trend follows well the trend earlier presented for the streamwise hub-height velocity.

As one could expect, the corresponding PSD of the RootFxc clearly illustrates both the influence of the background atmospheric flow as well as the influence of the actual rotating

blades. Results are presented in Figure 5.10 for a 90 m height turbine. This representation allows us to investigate which turbulent structures (associated to the corresponding frequencies) influence the most the RootFxc. For the SWT, under both CBL and NBL conditions, the corresponding RootFxc PSD is greatly influenced by the large eddies present in the background atmospheric flow (shown by the red box in Figure 5.10a). Similarly, this is observed for all three stratification conditions for the WF case. Interestingly, for the SWT during the SBL, the PSD of the RootFxc shows that the most energetic frequency is related to the frequency of the blades rotation, and it is not so much dependent on the background atmospheric flow. Peaks are observed at 1P, 2P, and 3P frequencies indicative of the influence of the rotation of the blades on the individual blade

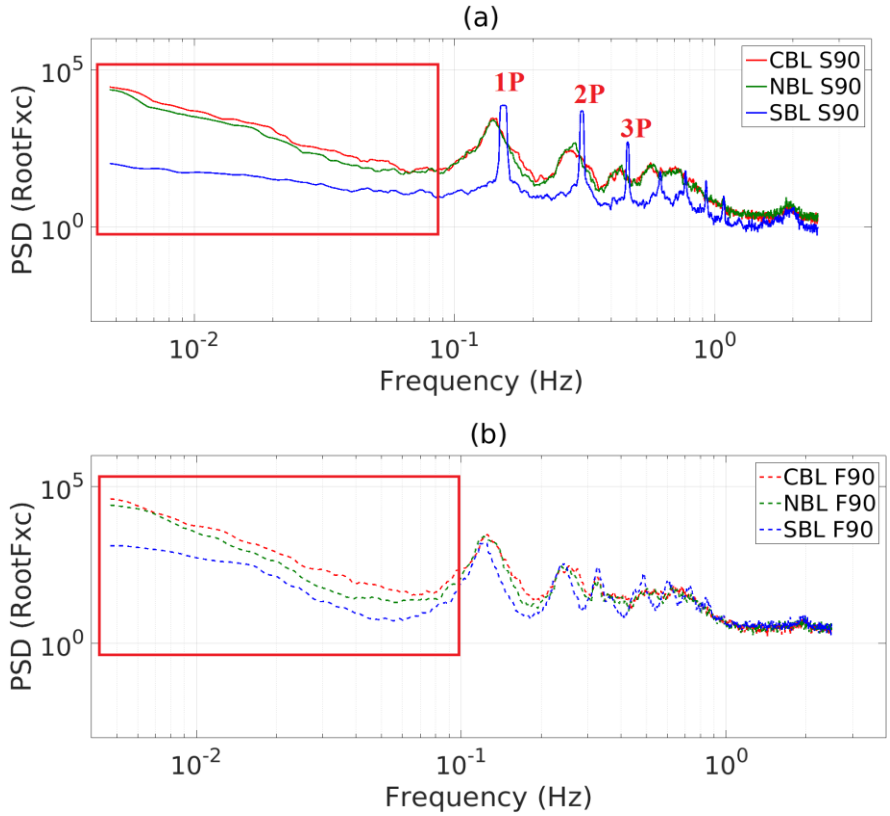

Figure 5.10. Power spectral density of RootFxc different stratifications, for (a) S90 and (b) F90 case.

loads, similar to the peaks observed in Figure 5.8. The peaks for a SWT under SBL conditions have a slight shift in the frequency as a result of the increased rotational speed. This same analysis has been developed for the different heights, and no relevant differences are observed. Only during the SBL for the SWT case, there exists a progressive shift of the peaks with respect to the frequency axis with increasing height, a result of the slight shift in rotational velocity previously observed in Figure 5.8.

5.5. Fore-aft shear force at the hub, Fxt (Rotor thrust)

The fore-aft shear force at hub-height, also known as the rotor thrust force, is the most important load acting on the wind turbine during operational time. It is the result of the aerodynamic, inertial, and gravitational forces, acting in the streamwise direction and at the turbine's hub. Figure 5.11 shows the variation of rotor thrust with respect to height, and for each wind turbine configuration and atmospheric stratification. For a SWT under CBL conditions, the mean rotor thrust is 325 KN, and the standard deviation is 120 KN. For the same stratification, a WF has a mean rotor thrust of 200 KN and the standard deviation is of the same value. This indicates that the rotor force fluctuates between 0 and 400 KN under this atmospheric stratification, hence strongly affecting the fatigue life of the turbine's structure. A similar trend is observed under the NBL for both the SWT and the WF cases, with a 10% reduction in both the mean and standard deviation. Under the SBL, the rotor thrust increases from 393 KN for a 90 m WT to 473 KN for a 150 m WT, a 20% increase. The standard deviation decreases from 9.5 KN at 90 m to 5.8 KN at 150 m for the WT case (40% decrease), indicating that the rotor thrust fluctuations decrease with increasing heights. This decrease may play an important role in the fatigue life of the wind

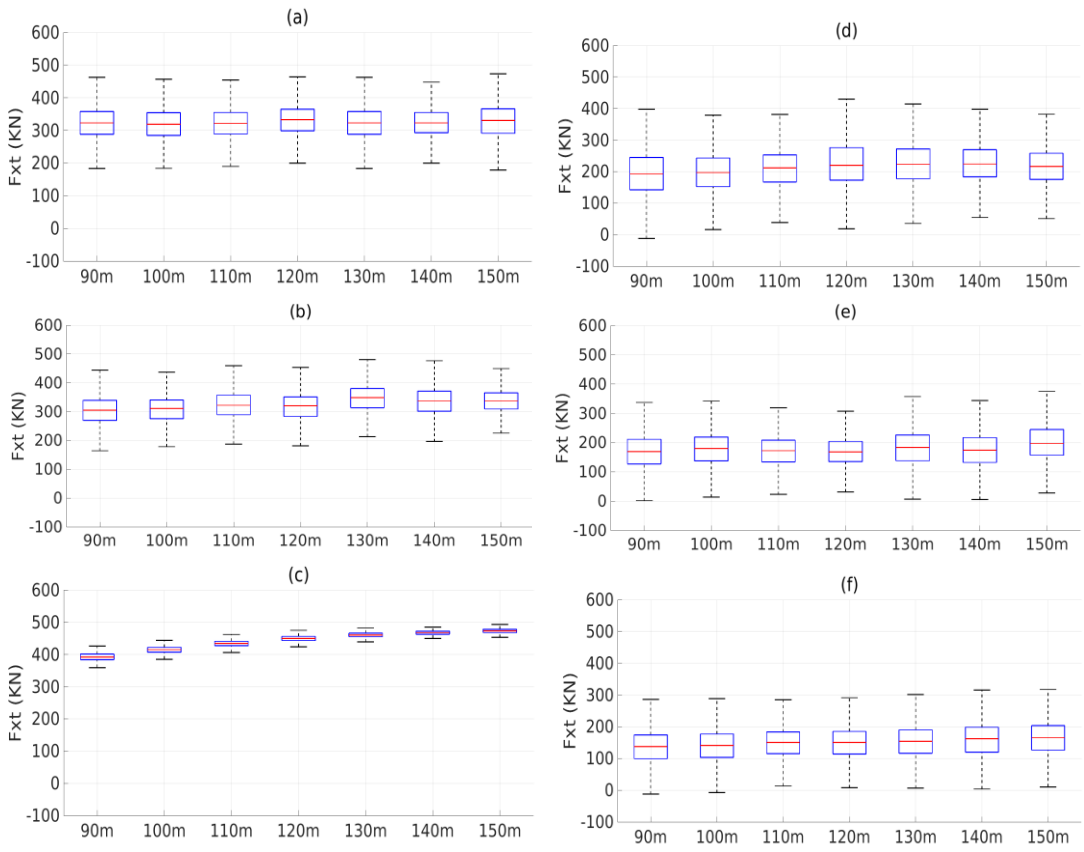

Figure 5.11. Box-plots representation rotor thrust, Fxt, for increasing heights for (a) SWT CBL (b) SWT NBL (c) SWT SBL (d) WF CBL (e) WF NBL (f) WF SBL cases.

turbine tower. Figure 5.12 presents the corresponding PSD for the rotor thrust (Fxt) for all the different cases. As previously seen in Figure 5.10, large eddies present in the turbulent wind field affect the frequencies of the rotor thrust for all cases other than the SWT under a SBL. The rotor thrust frequencies for the SWT under SBL are influenced largely by the rotational frequencies of the blades. A major difference in the PSD for the rotor thrust when compared to the PSD of the out-of plane shear at blade root (Figure 5.10) is that the first peak in the former occurs at around 0.36-0.48 Hz, which is three times the frequency of the individual blade loads. Hence, the peaks in the loads acting on the fixed frame are observed in harmonics of 3P, 6P, 9P, and so on in the PSD of the rotor

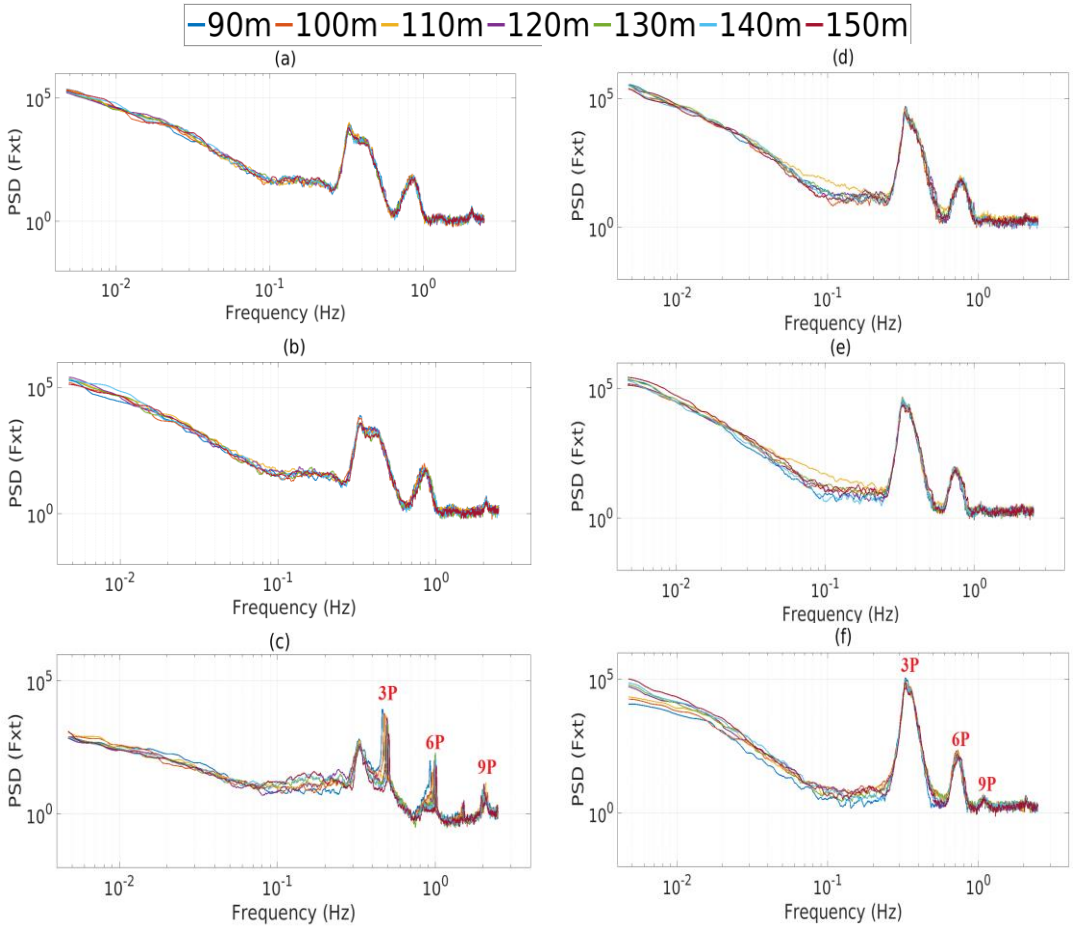

Figure 5.12. Power spectral densities of rotor thrust, Fxt for all tower heights for cases (a) SWT CBL (b) SWT NBL (c) SWT SBL (d) WF CBL (e) WF NBL (f) WF SBL.

thrust (see Figure 5.12 c and f).

5.6. Fore-aft bending moment at the hub, Myt

The fore-aft bending moment (Myt) at the hub is caused due to the combined effect of moment arising due to the aerodynamics, inertial, and gravitational loads, similar to the fore-aft shear force. It is interesting to see that Myt fluctuates between positive and negative values, and it is in the range of –2000 KN-m to 2000 KN-m for all the cases. This indicates that wind speed does not influence the fore-aft bending moment at the hub, contrary to the loads presented earlier (Figures 5.9, 5.11). As one could expect, the wind shear in front of

the rotor plays a very important role in determining the direction and amplitude of the fore-aft bending moment at the top of the turbine's tower. Figure 5.13 shows the variations of the fore-aft bending moment for all the different study cases. Under CBL conditions and for the SWT case, the mean fore-aft bending moment varies from -615 KN-m to -705 KN-m, with increasing heights having a standard deviation of around 2700 KN-m on average (subplot a). This means that the fore-aft bending moment constantly changes its direction with time. This is important because it plays an important role in the fatigue of the turbine's tower, especially at the top of the tower, where constant load reversals will occur. Similar

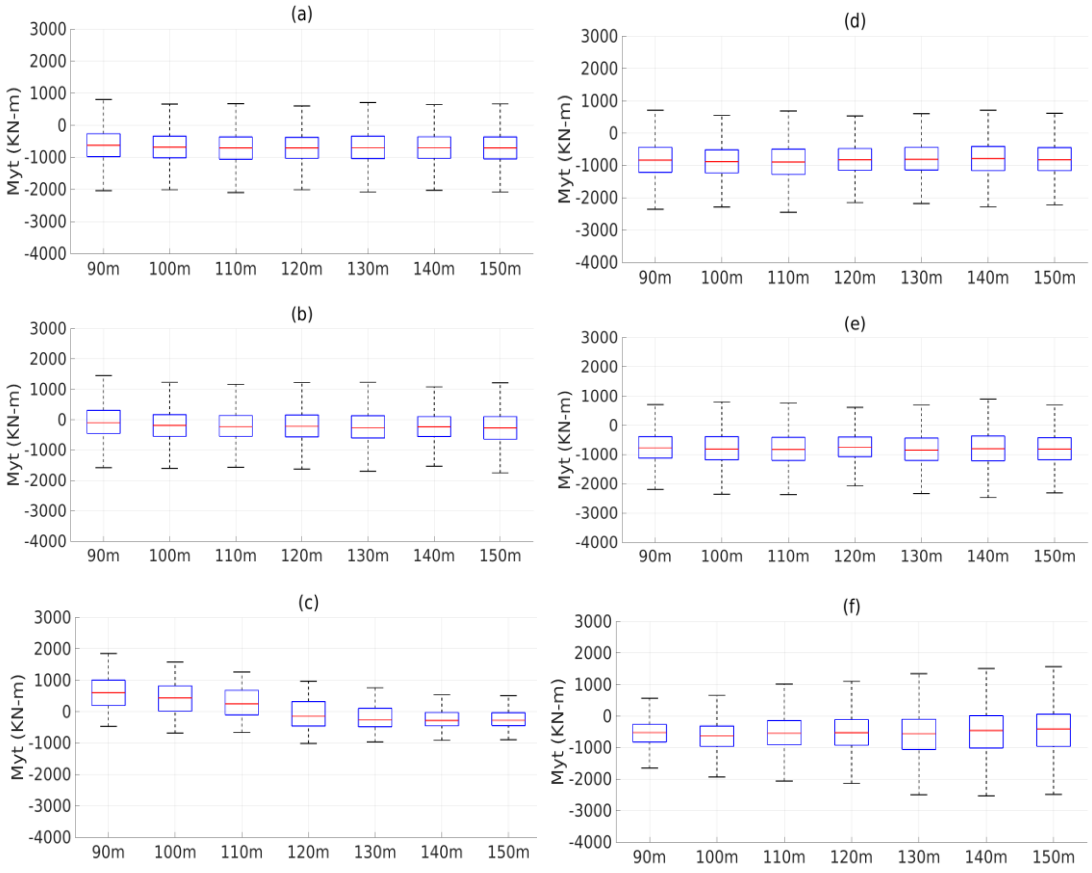

Figure 5.13. Box-plot representation of Myt for increasing heights for cases (a) SWT CBL (b) SWT NBL (c) SWT SBL (d) WF CBL (e) WF NBL (f) WF SBL.

trends are observed for the SWT case under NBL conditions, and the WF case under both CBL and NBL conditions (subplots b, d, and e). Positive mean values of the fore-aft bending moment are observed for the SWT under SBL conditions and for the 90 m, 100 m, and 110 m turbine tower heights (subplot c). The fore-aft bending moment decreases with turbine-height, from 605 KN-m to -236 KN-m, an effect of the decreasing wind shear as seen in section 5.1, Figure 5.3. For the WF case under SBL conditions, the fore-aft bending moment remains almost constant with an increase in height. When investigating the corresponding spectral distribution of the fore-aft bending moment, a similar patter to the one observed for the fore-aft shear force was observed (not included here for brevity).

5.7. Power

Because any wind turbine is designed with the sole purpose of harvesting wind power, here we investigate the differences and similitudes between the different study cases with respect to power extracted by the wind turbines. For the NREL onshore wind turbine, used in this study, the maximum rated power is 5 MW for a streamwise velocity ranging between 11.4 ms^{-1} and 25 ms^{-1}. In this study, the maximum streamwise velocity is always under the rated velocity of 11.4 ms^{-1}, hence the maximum power can never exceed the 5 MW. Figure 5.14 shows the box-plots for power output for all different study cases. A clear difference can be observed in the power outputs between the SWT and the WF cases. It is interesting to note that an increase in height does not produce a significant increase in power output for either of the cases, the SWT and the WF under CBL and NBL conditions. For the case of a SWT under SBL conditions, the power output increased from 1.8 MW to 2.4 MW, an increase of almost 30%. The LLJ observed during night time

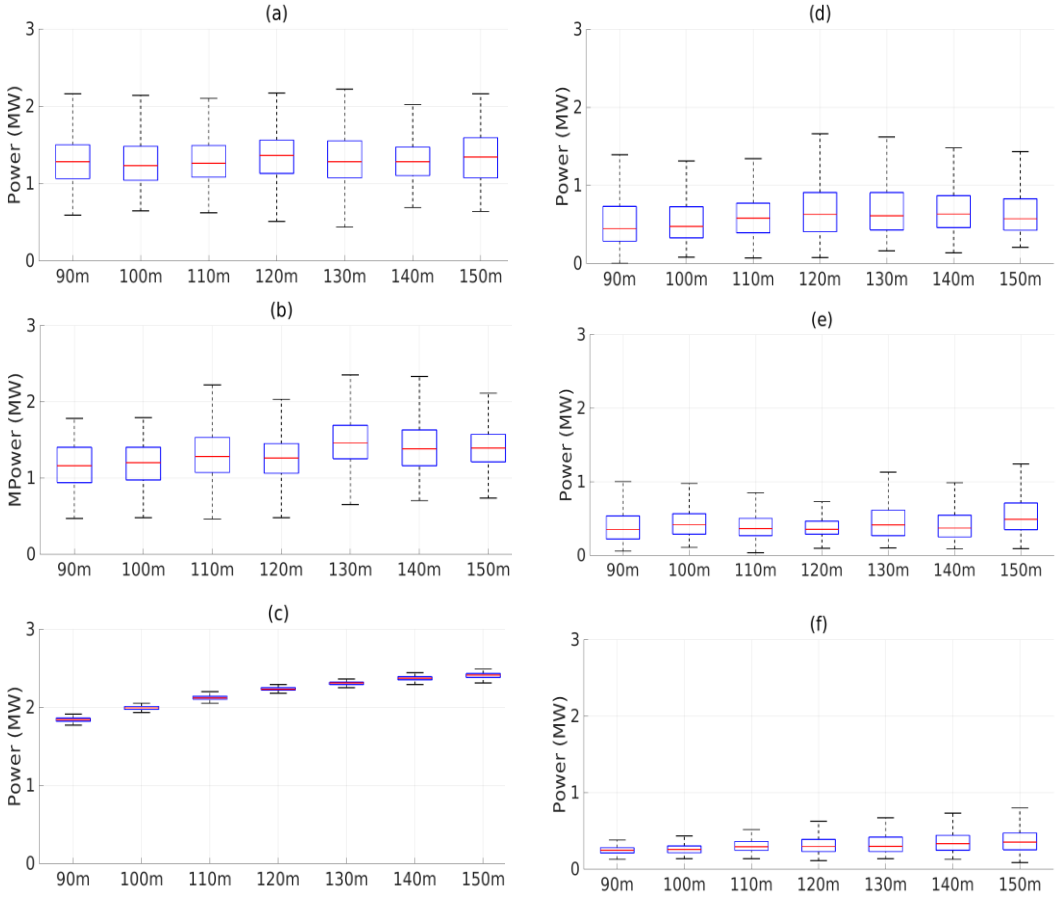

Figure 5.14. Box-plot representation for power output for increasing heights for (a) SWT CBL (b) SWT NBL (c) SWT SBL (d) WF CBL (e) WF NBL (f) WF SBL cases.

of only 0.245 MW, 7.5 times less than that produced for the same height for the single wind, interacts with the top portion of the blades (and bottom for wind turbines taller than 120 m) during the SWT case, leading to a strong increase in power. On the contrary, the lowest power output per turbine is observed for the WF case under SBL conditions, with a power output turbine case and 20 times below the rated power. This is a result of the vertical shift of the LLJ, as earlier mentioned in section 5.1 and also found in previous works (*68*). A detailed table with the power outputs can be found in Appendix A.

5.8. Tower loads

Figure 5.15 shows the tower loads for the SWT and the WF cases under the CBL, the NBL, and the SBL stratifications for all the different turbine heights. As can be observed, the tower loads range between 0.2 KN and 5.8 KN depending on the tower height and stratification. The reduction in wind speeds in front of the rotor area leads into a reduction in tower forces near the rotor. Maximum tower forces during the operational phase of a wind turbine would be observed in the lower third of the wind tower, as the velocities in front of the rotor plane are reduced due to the screen effect induced by the rotation of the blades. The fluctuations in the tower forces will naturally depend on the turbulence of the streamwise incoming wind. Hence, tower forces for the wind farm case would fluctuate

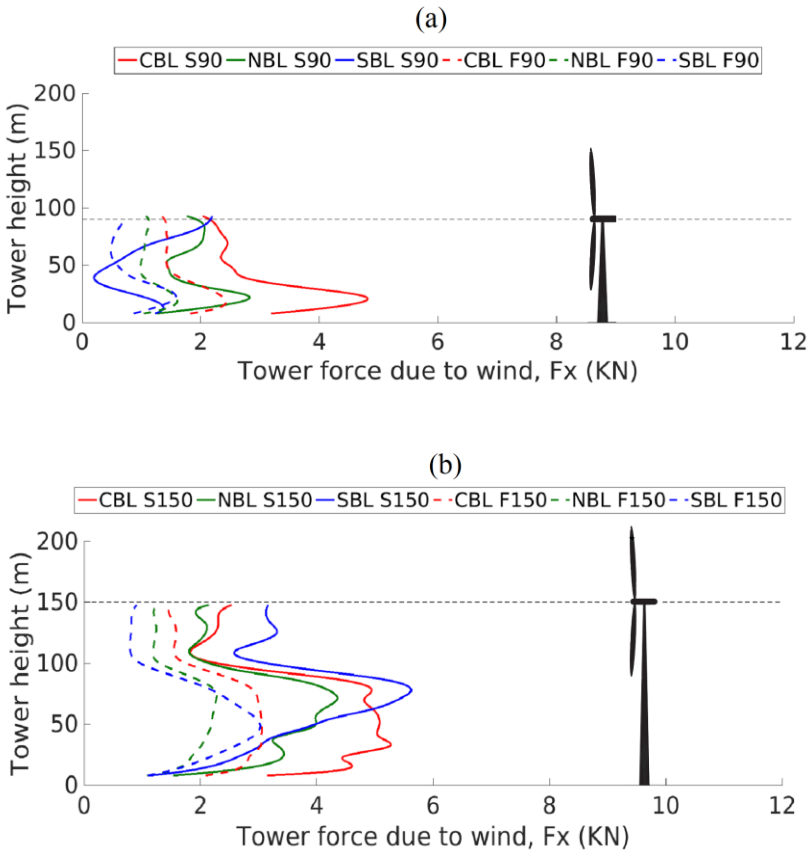

Figure 5.15. Tower forces due to wind, F_X for (a) 90 m tower (b) 150 m tower.

much more as compared to the single wind turbine. A noticeable increase of more than 100% is observed for the SWT under SBL (Figure 5.15). The intrusion of the low-level jet below the rotor for the 150 m turbine leads to this increased load of the tower (see Figure 5.2, b). However, tower forces are nearly 80 to 100 times smaller than the rotor thrust (see section 5.9), indicating that tower forces are negligible during an operational phase of the wind turbine as compared to the rotor forces.

5.9. Vertical distribution of the shear force and bending moment on turbine tower

The vertical distribution of the shear force and the bending moment in the streamwise direction on the turbine tower are computed for the all the study cases considering the tower to be a freestanding cantilever. Results help quantify and understand the influence of the rotor loads and tower loads on the shear force and bending moment on the tower. The resultant shear force variation along the tower height in the streamwise direction is shown in Figure 5.16 and it is a result of the combined effect of the rotor and tower loads. The plot shows a steep slope up to the hub-height, where the rotor thrust acts. This indicates that the rotor thrust is the most dominant force in the streamwise direction of the wind turbine, and more than 90% of the shear force is influenced due to the rotor thrust.

To complement these results, Figure 5.17 illustrates the variation in bending moment in the streamwise direction from the base to the top of the wind turbine tower. Significant increase can be observed at the base, from a 90 m wind turbine tower to a 150 m wind turbine tower. Also, an isolated wind turbine experiences almost a 2-fold increased base moment in comparison with the one experienced by a wind turbine placed in a wind farm,

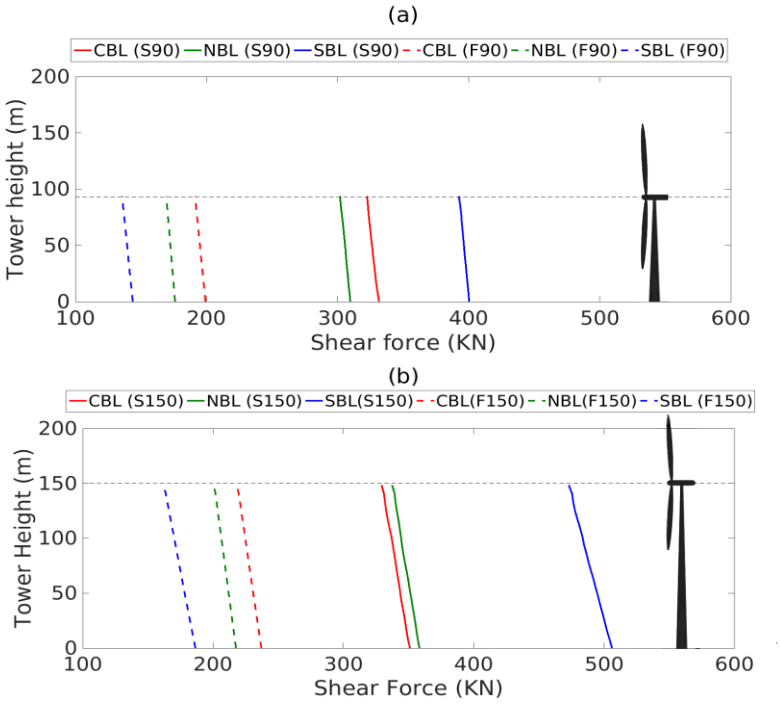

Figure 5.16. Shear force variation along tower heights for (a) 90 m tower (b) 150 m tower.

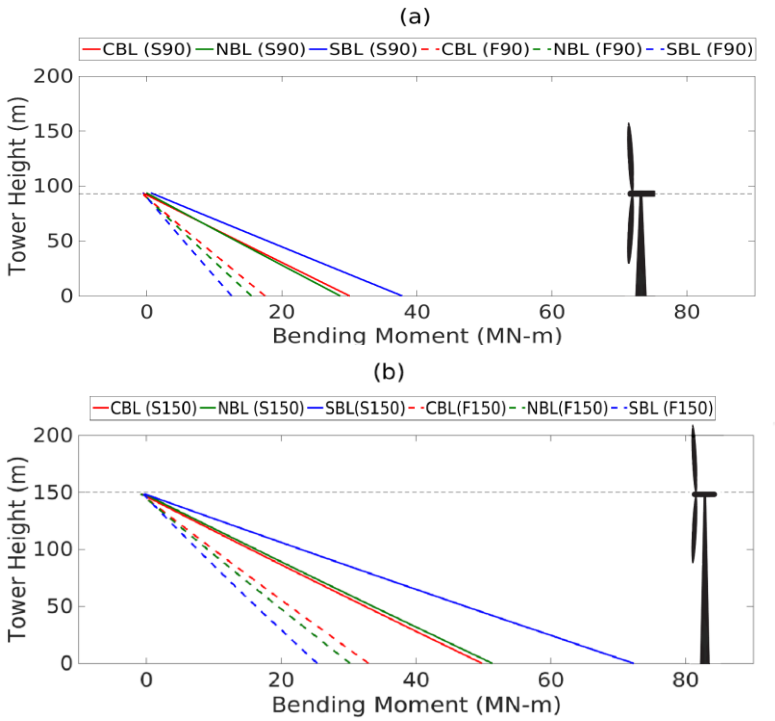

Figure 5.17. Streamwise bending moment variation along tower heights for (a) 90 m tower (b) 150 m tower.

for the same geostrophic wind. However, the former produces nearly 4 times as much power as compared to the latter (Appendix A). The results indicate that, for the same amount of bending moment, a single wind turbine produces twice the power as compared to a wind turbine in a wind farm.

.

CHAPTER 6

CONCLUSION

Within this master's thesis work, the diurnal evolution of a realistic atmospheric flow has been reproduced, within which wind turbines have been introduced, representing two different cases, an isolated wind turbine and the case of turbines within a very large wind farm. Isolated wind turbines are subject to stronger wind speeds and reduced turbulence when compared to wind farms, especially during atmospheric stable conditions. As a result, the loads experienced by the turbines are higher and the corresponding fluctuations are within 10% of the mean values. The turbines within large wind farms on the other hand experience lower wind speeds and higher turbulence levels. Hence, loads in wind farms are 50% smaller than those observed for the single wind turbine under the same geostrophic wind forcing. However, due to the increased turbulence in the wind, loads in the wind farm fluctuate around 25% of the mean, on average. Also, the experienced fluctuations increase with height, in the case of the WF under SBL conditions, and decrease with height for a SWT under the same stratification conditions. These fluctuations may play an important role in the fatigue life of the wind turbine structure and should be an interesting topic to be studied in the near future.

During the operational phase of the wind turbine, the rotor thrust is the most dominant force that acts on the wind turbine, tower forces being negligible in front of them. Results

have also shown that the rotor thrust is the most dominant force acting on the wind turbine during its operational phase and has the most influence on the shear and bending moment of the wind turbine tower. Rotor forces are nearly 80 to100 times larger than the individual tower forces. With these results, it is possible to conclude that aerodynamic tower designs will not lead to any considerable reduction in the base shear and base moment on the structure. Therefore, research should focus on obtaining a simplistic and practical design for the wind turbine tower using materials, easier to work with and transport, other than conventional steel.

Results have also shown the strong relevance of wind shear on the effect on the fore-aft bending moment at the hub (Myt). Higher wind shear leads to a positive value of Myt along the flow, whereas lower wind shear causes Myt to act in a direction opposite to the wind flow. A constant load reversal was observed for this moment at the hub of the wind tower. Also, the low-level jet tends to interact with the blades resulting in an enhanced wind speed and power in the case of a SWT. A significant increase in power output can be achieved by capturing the kinetic energy from the low-level jets in the case of a single wind turbine. According to our study, an increase in the tower heights for a wind turbine in a windfarm would not be the most efficient option in terms of power production

Increases in tower heights for the same blade size make a significant difference in terms of harvested power for the SWT case, especially during night time; however, minor differences are noted for the WF case. For the same geostrophic wind forcing, the maximum power generated by a single wind turbine is 2.4 MW, whereas for a wind turbine within a large wind farm, it is only about 0.65 MW, almost 4 times smaller. This indicates that building taller turbines in the case of very large wind farms may not be the best solution

for increasing power production. Staggered wind turbines with varying heights or heights increasing and decreasing alternatively for each row could be a viable option. According to our study, an increase in the tower heights for a wind turbine in a windfarm would not be the most efficient option in terms of power production.

In the near future, our research team plans to expand this research, and study the loads and power output for each row of turbines within a wind farm. Also, wind farms with staggered placements of wind turbines, and alternatively varying heights, will be studied. The LES framework is constantly being updated in order to obtain the highest spatial and temporal resolution. In future studies, a spatial resolution of 1 m and temporal resolution of 10 Hz should be achievable.

APPENDIX

Table A.1. Loads, shear force, bending moment, and power output for all cases.

Cases	RootFxc (KN)	Fxt (KN)	Myt (KN-m)	Base Shear (KN)	Base Moment (MN-m)	Power (MW)
CBL S90	133.728	322.537	-615.9125	331.6629	30.045	1.2923
NBL S90	126.565	301.898	-59.6905	309.7159	28.646	1.1586
SBL S90	158.497	392.540	605.0525	400.3614	37.823	1.8390
CBL F90	88.323	191.364	-817.945	199.2631	17.251	0.517
NBL F90	80.727	169.353	-722.1819	176.1102	15.485	0.400
SBL F90	69.289	135.798	-553.1956	143.8547	12.577	0.245
CBL S100	133.068	320.677	-672.738	333.3096	32.44	1.2788
NBL S100	127.8	305.841	-173.989	314.8108	31.325	1.1830
SBL S100	166.536	414.755	427.1865	427.3379	43.194	1.9905
CBL F100	90.568	197.399	-884.7841	208.3264	19.708	0.541
NBL F100	83.701	177.909	-753.6737	186.4626	17.746	0.435
SBL F100	70.593	139.541	-636.0188	151.3025	14.108	0.261
CBL S110	133.467	321.8192	-709.232	337.3325	38.946	1.3492
NBL S110	133.1961	321.1972	-197.956	333.1088	37.501	1.2541
SBL S110	173.417	433.684	282.7285	448.8781	53.733	2.2309
CBL F110	95.541	209.363	-887.7104	221.5170	22.667	0.599
NBL F110	81.527	171.5145	-809.8315	181.1846	18.472	0.406
SBL F110	73.464	147.987	-539.0287	161.7651	16.369	0.299

Table A.1 Continued

CBL S120	136.372	330.529	-700.192	347.0109	38.946	1.3492
NBL S120	131.416	315.6936	-195.472	327.876	37.501	1.2541
SBL S120	179.1343	449.574	-76.2815	468.5324	53.733	2.2309
CBL F120	100.405	226.372	-797.2947	240.2259	26.524	0.705
NBL F120	81.233	170.752	-713.8196	182.0480	19.94	0.398
SBL F120	73.186	149.926	-553.8191	167.2452	17.994	0.313
CBL S130	134.062	323.5515	-684.496	341.1199	43.139	1.3056
NBL S130	141.458	344.387	-227.223	358.2359	46.470	1.4501
SBL S130	183.0763	460.091	-192.5054	483.5164	62.464	2.3108
CBL F130	100.294	225.9721	-780.382	240.2211	30.209	0.696
NBL F130	85.392	182.653	-798.3381	195.0736	24.326	0.466
SBL F130	74.898	152.095	-602.3471	170.4645	20.845	0.322
CBL S140	135.347	327.360	-690.714	347.2148	46.729	1.3268
NBL S140	138.743	337.404	-213.747	353.698	48.386	1.3983
SBL S140	185.833	467.589	-241.0566	496.2608	67.5	2.3674
CBL F140	101.413	229.026	-778.0295	245.0374	32.599	0.717
NBL F140	82.834	175.189	-758,4704	189.188	24.902	0.428
SBL F140	76.699	157.471	-510.8871	177.7288	23.086	0.348
CBL S150	136.177	329.258	-706.2152	351	49.77	1.3418
NBL S150	138.871	337.390	-266.988	358.4	51.3	1.3994
SBL S150	187.641	427.88	-236.194	506.1	72.25	2.4058
CBL F150	97.639	218.118	-801.0481	237.1	32.85	0.649
NBL F150	91.511	200.478	-791.8629	217.6	30.21	0.559
SBL F150	78.238	161.922	-453.516	186.5	25.34	0.370

REFERENCES

1. Burton, T.; Sharpe, D.; Jenkins N. *Handbook of wind energy*; John Wiley & Sons: Chichester, **2001**.

2. *State of the Climate: Global Analysis - December 2014*. NOAA National Centers for Environmental Information, U.S. Department of Commerce, Washington D.C., **2015**. http://www.ncdc.noaa.gov/sotc/global/201412 (accessed Nov 9, 2015).

3. *Wind Vision: A New Era for Wind Power in the United States*. Technical report, U.S. Department of Energy, Washington D.C., **2015**.

4. *U.S. Installed Wind Capacity*. WINDExchange, U.S. Department of Energy, Washington D.C., **2015**. http://apps2.eere.energy.gov/wind/windexchange/wind_installed_capacity.asp (accessed Nov 15, 2015).

5. *Turbine Timeline: The History of AWEA and the U.S. Wind Industry*. American Wind Energy Association, Washington D.C., **2015**. http://www.awea.org/Content.aspx?ItemNumber=771 (accessed Apr 15, 2016).

6. Lanchester, F. W. A contribution to the theory of propulsion and the screw propeller. *Journal of the American Society for Naval Engineers* **2009**, *27* (2), 509–510.

7. Glauert, H. Airplane propellers. *Aerodynamic Theory* **1935**, 169–360.

8. Gaonkar, G. H.; Peters, D. A. Effectiveness of Current Dynamic-Inflow Models in Hover and Forward Flight. *Journal of the American Helicopter Society* **1986**, *31* (2), 47–57.

9. Van Bussel G.J.W. Effectiveness of Current Dynamic-Inflow Models in Hover and Forward Flight. *European Wind Energy Conference* **1994**, p. 834–9.

10. Hansen, C. Aerodynamics of horizontal-axis wind turbines. *Annual Review of Fluid Mechanics* **1993**, *25* (1), 115–149.

11. Benini, E.; Toffolo, A. Optimal design of horizontal-axis wind turbines using blade-element theory and evolutionary computation. *Journal of Solar Energy Engineering* **2002**, *124* (4), 357.

12. Islam, M.; Ting, D.; Fartaj, A. Aerodynamic models for Darrieus-type straight-bladed vertical axis wind turbines. *Renewable and Sustainable Energy Reviews* **2008**, *12* (4), 1087–1109.

13. Xudong, W.; Shen, W. Z.; Zhu, W. J.; Sørensen, J. N.; Jin, C. Shape optimization of wind turbine blades. *Wind Energy* **2009**, *12* (8), 781–803.

14. Vermeer, L.; Sørensen, J.; Crespo, A. Wind turbine wake aerodynamics. *Progress in Aerospace Sciences* **2003**, *39* (6-7), 467–510.

15. Crespo, A.; Hernandez, J. Turbulence characteristics in wind-turbine wakes. *Journal of Wind Engineering and Industrial Aerodynamics* **1996**, *61* (1), 71–85.

16. Whale, J.; Anderson, C.; Bareiss, R.; Wagner, S. An experimental and numerical study of the vortex structure in the wake of a wind turbine. *Journal of Wind Engineering and Industrial Aerodynamics* **2000**, *84* (1), 1–21.

17. Ivanova, L. A.; Nadyozhina, E. D. Wind flow deformation inside the wind farm. *Journal of Wind Engineering and Industrial Aerodynamics* **1998**, *74-76*, 389–397.

18. Ebert, P.; Wood, D. The near wake of a model horizontal-axis wind turbine—I. Experimental arrangements and initial results. *Renewable Energy* **1997**, *12* (3), 225–243.

19. Magnusson, M.; Smedman, A.S. Air flow behind wind turbines. *Journal of Wind Engineering and Industrial Aerodynamics* **1999**, *80* (1-2), 169–189.

20. Sørensen, J.N.; Shen, W. Z. Numerical modeling of wind turbine wakes. *Journal of Fluids Engineering* **2002**, *124* (2), 393.

21. Lissaman, P. B. S. Energy effectiveness of arbitrary arrays of wind turbines. *Journal of Energy* **1979**, *3* (6), 323–328.

22. Katic, I.; Højstrup, J.; Jensen, N.O. A simple model for cluster efficiency. *European Wind Energy Association Conference and Exhibition* **1986**, 407-410.

23. Mosetti, G.; Poloni, C.; Diviacco, B. Optimization of wind turbine positioning in large windfarms by means of a genetic algorithm. *Journal of Wind Engineering and Industrial Aerodynamics* **1994**, *51* (1), 105–116.

24. Grady, S.; Hussaini, M.; Abdullah, M. Placement of wind turbines using genetic algorithms. *Renewable Energy* **2005**, *30* (2), 259–270.

25. Chen, Y.; Li, H.; Jin, K.; Song, Q. Wind farm layout optimization using genetic algorithm with different hub height wind turbines. *Energy Conversion and Management* **2013**, *70*, 56–65.

26. Bechly, M.; Clausen, P. Structural design of a composite wind turbine blade using finite element analysis. *Computers & Structures* **1997**, *63* (3), 639–646.

27. Ong, C.H.; Stephen W. T. *The use of carbon fibers in wind turbine blade design: a SERI-8 blade example*. *No. SAND2000-0478*. Sandia National Labs., Albuquerque, NM (US); Sandia National Labs., Livermore, CA (US), **2000**.

28. Kong, C.; Bang, J.; Sugiyama, Y. Structural investigation of composite wind turbine blade considering various load cases and fatigue life. *Energy* **2005**, *30* (11-12), 2101–2114.

29. Jensen, F.; Falzon, B.; Ankersen, J.; Stang, H. Structural testing and numerical simulation of a 34m composite wind turbine blade. *Composite Structures* **2006**, *76* (1-2), 52–61.

30. Jay, A.; Myers, A. Design of Conical Steel Wind Turbine Towers Manufactured with Automated Spiral Welding. *Structures Congress* **2014**, 1675-1683.

31. Sritharan, S.; Grant, M. S. Design of tall wind turbine towers utilizing UHPC. *RILEM-fib-AFGC International Symposium On Ultra-High Performance Reinforced Concrete, Marseille, France* **2013**, 433-442.

32. Quilligan, A.; O'Connor, A.; Pakrashi, V. Fragility analysis of steel and concrete wind turbine towers. *Engineering Structures* **2012**, *36*, 270–282.

33. Gibson, M. M.; Launder, B. E. Ground effects on pressure fluctuations in the atmospheric boundary layer. *Journal of Fluid Mechanics* **1978**, *86* (03), 491.

34. Garratt, J. R. *The atmospheric boundary layer*; Cambridge University Press: Cambridge, **1992**, 444.

35. Kaimal, J.C.; Finnigan, J.J. *Atmospheric boundary layer flows: their structure and measurement*. Oxford University Press, **1994**.

36. Smagorinsky, J. General circulation experiments with the primitive equations: I. the basic experiment. *Monthly Weather Review* **1963**, *91* (3), 99–164.

37. Deardorff, J. W. Numerical investigation of neutral and unstable planetary boundary layers. *Journal of the Atmospheric Sciences* **1972**, *29* (1), 91–115.

38. Deardorff, J. Three-dimensional numerical study of the height and mean structure of a heated planetary boundary layer. *Boundary-Layer Meteorology* **1974**, *7* (1).

39. Germano, M.; Piomelli, U.; Moin, P.; Cabot, W. H. A dynamic subgrid-scale eddy viscosity model. *Physics of Fluids A: Fluid Dynamics* **1991**, *3* (7), 1760.

40. Lilly, D. K. A proposed modification of the Germano subgrid-scale closure method. *Physics of Fluids A: Fluid Dynamics* **1992**, *4* (3), 633.

41. Sim, C.; Basu, S.; Manuel, L. On space-time resolution of inflow representations for wind turbine Loads Analysis. *Energies* **2012**, *5* (12), 2071–2092.

42. Park, J.; Basu, S.; Manuel, L. Large-eddy simulation of stable boundary layer turbulence and estimation of associated wind turbine loads. *Wind Energy* **2013**, *17* (3), 359–384.

43. Park, J.; Manuel, L.; Basu, S. Toward isolation of Salient features in stable boundary layer wind fields that influence loads on wind turbines. *Energies* **2015**, *8* (4), 2977–3012.

44. International Electrotechnical Commission. *Wind Turbine Generator System Part 1: Design Requirements*. IEC 61400-1, Edition 3.0, **2005**.

45. Malcolm, D. J. *WindPACT rotor design study: hybrid tower design*; National Renewable Energy Laboratory: Golden, CO, **2004**.

46. Oke, T. R. *Boundary layer climates*; Methuen: London, **1978**.

47. Stull, R. B. *An introduction to boundary layer meteorology*; Kluwer Academic Publishers: Dordrecht, **1988**.

48. Arya, S. P. *Introduction to micrometeorology*; Academic Press: San Diego, **1988**.

49. *Minimum design loads for buildings and other structures*; American Society of Civil Engineers: Reston, VA, **2010**.

50. *International building code: 2012*; International Code Council: Country Club Hills, IL, **2012**.

51. Rife, D. L.; Pinto, J. O.; Monaghan, A. J.; Davis, C. A.; Hannan, J. R. Global distribution and characteristics of diurnally varying low-level jets. *Journal of Climate* **2010**, *23* (19), 5041–5064.

52. Pope, S. B. *Turbulent flows*; Cambridge University Press: Cambridge, **2000**.

53. Sharma, V.; Calaf, M.; Lehning, M.; Parlange, M. B. Time-adaptive wind turbine model for an LES framework. *Wind Energy* **2015**, *19* (5), 939–952.

54. Orszag, S. A.; Pao, Y.H. Numerical computation of turbulent shear flows. *Advances in Geophysics* **1975**, 225–236.

55. Bou-Zeid, E.; Meneveau, C.; Parlange, M. A scale-dependent Lagrangian dynamic model for large-eddy simulation of complex turbulent flows. *Physics of Fluids* **2005**, *17* (2), 025105.

56. Calaf, M.; Parlange, M. B.; Meneveau, C. Large eddy simulation of scalar transport in fully developed wind-turbine array boundary layers. *Physics of Fluids* **2011**, *23* (12), 126603.

57. Moeng, C.H. A large-eddy simulation model for the study of planetary boundary-layer turbulence. *Journal of the Atmospheric Sciences* **1984**, *41* (13), 2052–2062.

58. Albertson, J. D.; Parlange, M. B. Natural integration of scalar fluxes from complex terrain. *Advances in Water Resources* **1999**, *23* (3), 239–252.

59. Albertson, J. D.; Parlange, M. B. Surface length-scales and shear stress: implications for land-atmosphere interaction over complex terrain. *Water Resources Research* **1999**, *35* (7), 2121–2132.

60. Canuto, C.; Hussaini, M. Y.; Quarteroni, A.; Zang, T. A. *Spectral Methods in Fluid Dynamics*; Springer-Verlag: Berlin, **1988**.

61. Brutsaert, W.; Parlance, M. B. The unstable surface layer above forest: regional evaporation and heat flux. *Water Resources Research* **1992**, *28* (12), 3129–3134.

62. Brutsaert, W. *Hydrology: an introduction*; Cambridge University Press: Cambridge, **2005**.

63. Brutsaert, W.; Parlange M.B.; Gash J.H.C. Neutral humidity profiles in the boundary layer and regional evaporation from sparse pine forest. *Annales Geophysicae* **1989**, *7*, 623-630.

64. Jonkman, J. M.; Buhl, M. L. *FAST user's guide: updated August 2005*; National Renewable Energy Laboratory: Golden, CO, **2005**.

65. LaNier, M.W. *LWST Phase I Project Conceptual Design Study: Evaluation of Design and Construction Approaches for Economical Hybrid Steel/Concrete Wind Turbine Towers*; *June 28, 2002 – July 31, 2004.* NREL/SR-500-36777, National Renewable Energy Laboratory, Golden, CO, **2004.**

66. Jonkman, J.M.; Butterfield, S.; Musical, W.; Scott, G. *Definition of a 5MW reference wind turbine for offshore system development*. Technical Report NREL/TP-500-38060, National Renewable Energy Laboratory, Golden, CO, **2007**.

67. Kumar, V.; Svensson, G.; Holtslag, A. A. M.; Meneveau, C.; Parlange, M. B. Impact of surface flux formulations and geostrophic forcing on large-eddy simulations of diurnal atmospheric boundary layer flow. *Journal of Applied Meteorology and Climatology* **2010**, *49* (7), 1496–1516.

68. Fitch, A. C.; Olson, J. B.; Lundquist, J. K.; Dudhia, J.; Gupta, A. K.; Michalakes, J.; Barstad, I. Local and mesoscale impacts of wind farms as parameterized in a mesoscale NWP model. *Monthly Weather Review* **2012**, *140* (9), 3017–3038.